



# REST-UV ABSORPTION LINES AS METALLICITY ESTIMATOR: THE METAL CONTENT OF STAR-FORMING GALAXIES AT $z \sim 5$

A. L. FAISST<sup>1,2,12</sup>, P. L. CAPAK<sup>1,2</sup>, I. DAVIDZON<sup>3,4</sup>, M. SALVATO<sup>5</sup>, C. LAIGLE<sup>6</sup>, O. ILBERT<sup>3</sup>, M. ONODERA<sup>7</sup>, G. HASINGER<sup>8</sup>, Y. KAKAZU<sup>9</sup>, D. MASTERS<sup>1,2</sup>, H. J. MCCrackEN<sup>6</sup>, B. MOBASHER<sup>10</sup>, D. SANDERS<sup>8</sup>, J. D. SILVERMAN<sup>11</sup>, L. YAN<sup>1</sup>, AND N. Z. SCOVILLE<sup>2</sup>

<sup>1</sup> Infrared Processing and Analysis Center, California Institute of Technology, Pasadena, CA 91125, USA; [afaisst@ipac.caltech.edu](mailto:afaisst@ipac.caltech.edu)

<sup>2</sup> Cahill Center for Astronomy and Astrophysics, California Institute of Technology, Pasadena, CA 91125, USA

<sup>3</sup> Aix Marseille Université, CNRS, LAM (Laboratoire d’Astrophysique de Marseille) UMR 7326, F-13388, Marseille, France

<sup>4</sup> INAF—Osservatorio Astronomico di Bologna, via Ranzani 1, I-40127, Bologna, Italy

<sup>5</sup> Max Planck Institut für Extraterrestrische Physik, Giessenbachstrasse 1, D-85748, Garching bei München, Germany

<sup>6</sup> Institut d’Astrophysique de Paris, CNRS & UPMC, UMR 7095, 98 bis Boulevard Arago, F-75014, Paris, France

<sup>7</sup> Institute for Astronomy, Swiss Federal Institute of Technology, 8093 Zürich, Switzerland

<sup>8</sup> Institute for Astronomy, 2680 Woodlawn Dr., University of Hawaii, Honolulu, HI 96822, USA

<sup>9</sup> Subaru Telescope, 650 N. A’ohoku Place, Hilo, HI 96720, USA

<sup>10</sup> Department of Physics and Astronomy, University of California, Riverside, CA 92521, USA

<sup>11</sup> Kavli Institute for the Physics and Mathematics of the universe (WPI), The University of Tokyo Institutes for Advanced Study,

The University of Tokyo, Kashiwa, Chiba 277-8583, Japan

Received 2015 November 19; accepted 2016 February 13; published 2016 May 2

## ABSTRACT

We measure a relation between the depth of four prominent rest-UV absorption complexes and metallicity for local galaxies and verify it up to  $z \sim 3$ . We then apply this relation to a sample of 224 galaxies at  $3.5 < z < 6.0$  ( $\langle z \rangle = 4.8$ ) in the Cosmic Evolution Survey (COSMOS), for which unique UV spectra from the Deep Imaging Multi-object Spectrograph (DEIMOS) and accurate stellar masses from the *Spitzer Large Area Survey with Hyper-Suprime-Cam* (SPLASH) are available. The average galaxy population at  $z \sim 5$  and  $\log(M/M_\odot) > 9$  is characterized by 0.3–0.4 dex (in units of  $12 + \log(\text{O}/\text{H})$ ) lower metallicities than at  $z \sim 2$ , but comparable to  $z \sim 3.5$ . We find galaxies with weak or no Ly $\alpha$  emission to have metallicities comparable to  $z \sim 2$  galaxies and therefore may represent an evolved subpopulation of  $z \sim 5$  galaxies. We find a correlation between metallicity and dust in good agreement with local galaxies and an inverse trend between metallicity and star-formation rate consistent with observations at  $z \sim 2$ . The relation between stellar mass and metallicity (MZ relation) is similar to  $z \sim 3.5$ , but there are indications of it being slightly shallower, in particular for the young, Ly $\alpha$ -emitting galaxies. We show that, within a “bathtub” approach, a shallower MZ relation is expected in the case of a fast (exponential) build-up of stellar mass with an  $e$ -folding time of 100–200 Myr. Because of this fast evolution, the process of dust production and metal enrichment as a function of mass could be more stochastic in the first billion years of galaxy formation compared to later times.

*Key words:* galaxies: abundances – galaxies: evolution – galaxies: high redshift – galaxies: ISM

## 1. INTRODUCTION

Metallicity is an important diagnostic for understanding the details of galaxy formation because its connection to the history of a galaxy’s star-formation rate (SFR), including gas inflow and outflow, that is, the interplay between the interstellar medium (ISM) and the intergalactic medium (IGM). While the metal content of galaxies and its relation to other physical properties has been studied in depth at  $z \sim 2$ –3, there are only a handful of observations at higher redshifts.

The presence of a tight relation (0.07–0.20 dex scatter) between the galaxy’s stellar mass and gas-phase metallicity (the MZ relation), measured by the ratio of oxygen to hydrogen,<sup>12</sup> was seen in local galaxies as early as the 1970s (Lequeux et al. 1979, see also Bothwell et al. 2013). Recently improved instrumental capabilities in the near-infrared (near-IR) that allow the measurement of metallicity at higher redshifts show that this relation holds up to  $z \sim 2$  (Maier et al. 2005, 2015; Savaglio et al. 2005; Erb et al. 2006; Maiolino et al. 2008; Roseboom et al. 2012; Henry et al. 2013; Gallazzi et al. 2014;

Wuyts et al. 2014; Salim et al. 2015; Sanders et al. 2015b) and even up to  $z \sim 3$ , although only in small sample sizes (Mannucci et al. 2009; Belli et al. 2013; Maier et al. 2014; Onodera et al. 2016). At all redshifts, the metal content of galaxies is observed to increase with increasing stellar mass but flattens out above a stellar mass of roughly  $\log(M/M_\odot) = 10.0$ –10.5. The MZ relation is also observed to evolve with redshift, with galaxies at high redshifts showing a lower metal content. Galaxies at  $z \sim 3$  are found to have only about one-fifth of the solar metal abundance (Mannucci et al. 2009; Jones et al. 2012; Onodera et al. 2016). Besides the correlation of metallicity with stellar mass and cosmic time, an *inverse* dependence with SFR has been found in local galaxies (Ellison et al. 2008; Lara-López et al. 2010; Andrews & Martini 2013). This has led to the so-called “fundamental mass–metallicity relation” (see Mannucci et al. 2010), but the universality of this three-dimensional relation is debated as there is evidence of it breaking down at  $z \sim 2$ –3 (see, e.g., Maier et al. 2014; Salim et al. 2015).

Several physical processes have been suggested for the origin of the MZ relation. For example, the deficit of metals in low-mass galaxies can be attributed to strong winds (stellar winds or supernovae feedback) that excavate metal-rich gas out

<sup>12</sup> Twitter: @astrofaisst.

<sup>13</sup> We define the solar metallicity as  $Z_\odot = 0.02$ .

of the galaxy’s low gravitational potential (e.g., Larson 1974; Edmunds 1990; Garnett 2002; De Lucia et al. 2004; Tremonti et al. 2004; Finlator & Davé 2008). Such strong outflows are found to be ubiquitous in local starburst galaxies as well as star-forming galaxies at higher redshifts (e.g., Steidel et al. 2010; Kornei et al. 2012; Martin et al. 2012). Also, more massive galaxies tend to form their stars earlier (an effect called “downsizing,” e.g., Cowie et al. 1996; Gavazzi & Scodreggio 1996; Franceschini et al. 2006; Pérez-González et al. 2008; Ilbert et al. 2013) and therefore start to enrich their ISM earlier than less massive galaxies. It is also important to mention that the shape of the initial stellar mass function (IMF) affects the rate at which the ISM gets enriched by metals and thus has a direct influence on the shape of the MZ relation (e.g., Köppen et al. 2007). The evolution of metallicity with cosmic time and its dependence on stellar mass and SFR has been successfully predicted by semiempirical models under the assumption that the metal content in the ISM is set by the balance between the inflow of pristine (i.e., metal-poor) gas and enrichment through star formation. (see Bouché et al. 2010; Davé et al. 2012; Lilly et al. 2013; Pipino et al. 2014; Feldmann 2015; Harwit & Brisbin 2015).

The gas-phase metallicity of a galaxy is commonly derived from the ratio between strong emission line features in the optical part of the spectrum ([O II], [O III], H $\alpha$ , H $\beta$ , [N II]) calibrated to theoretical models (e.g., Kewley & Dopita 2002; Nagao et al. 2006; Kewley & Ellison 2008; Maiolino et al. 2008). The most common of these so-called “strong-line methods” include the  $R_{23}$  diagnostics (combining [O III], [O II], and H $\beta$ ; Pagel et al. 1979) and the N2 method (combining H $\alpha$  and [N II]; Storch-Bergmann et al. 1994), which is commonly used to break the degeneracy and dust dependence of the  $R_{23}$  method. While the strong-line methods can be employed up to  $z \sim 3$ , at higher redshifts the diagnostic lines fall out of the wavelength window of ground-based near-IR spectrographs. This considerably hampers the investigation of the metal content of galaxies at very early epochs and therefore our understanding of the formation of these galaxies, until the advent of the *James Webb Space Telescope* (JWST).

A correlation between metallicity and the equivalent width (EW) of absorption features in the rest-frame ultraviolet (UV) is expected from theoretical models (e.g., Eldridge & Stanway 2012) and is observed in starburst galaxies in the local universe (e.g., Heckman et al. 1998; Rix et al. 2004; Leitherer et al. 2011; James et al. 2014). It provides an alternative way to probe statistically the metal content of galaxies. This method has already been used to determine stellar and gas-phase metallicities of  $z \sim 3$  galaxies, returning reasonable results (e.g., Mehlert et al. 2002; Savaglio et al. 2004; Maraston et al. 2009; Sommariva et al. 2012). However, this correlation has never been directly verified to hold at high redshifts.

In this paper, we aim (1) to verify the relation between EW and metallicity at high redshift and (2) use it to investigate the metal content of 224 star-forming galaxies at  $z \sim 5$  with rest-frame UV spectra obtained by the Deep Imaging Multi-object Spectrograph (DEIMOS; Faber et al. 2003). The large sample size allows us to investigate the dependence of metallicity on stellar mass for the first time at these early epochs, giving us clues on how these galaxies are formed.

The paper is organized as follows. We first verify the relation between EW and metallicity of local galaxies on a sample of  $z \sim 2$ –3 galaxies (Section 2). We then present in Section 3 the

sample of  $z \sim 5$  galaxies to which we will apply this relation to estimate their metallicities. In Section 4 we present the  $z \sim 5$  composite spectrum and describe the measurement of EWs, including the correction for various biases. The results of our analysis are presented in Section 5. Eventually, in Section 6, we discuss the metal content of  $z \sim 5$  galaxies and conclude and summarize the results of this paper in Section 7.

We adopt a flat cosmology with  $\Omega_{\Lambda,0} = 0.7$ ,  $\Omega_{m,0} = 0.3$ , and  $h = 0.7$ . Magnitudes are given in the AB system (Oke & Gunn 1983), and stellar masses are computed for a Chabrier (2003) initial mass function (IMF). Metallicities are quoted in the calibration of Maiolino et al. (2008).<sup>14</sup>

## 2. UV ABSORPTION LINES AS A MEASURE OF METALLICITY

The strong-line methods, based on the ratio of strong optical emission lines to determine gas-phase metallicities, work well up to a redshift of  $z \sim 3$ . Above that, the lines are shifted out of the wavelength range of current ground-based near-IR spectrographs. An alternative way to estimate metallicity is to use its relation with the EW of IS, photometric, and wind-dominated absorption features in the rest-frame UV. In this section, we calibrate this relation using a set of local galaxies and verify it at redshifts as high as  $z \sim 3$  before applying it to a sample of  $z \sim 5$  galaxies.

There are several physical aspects that could cause a correlation between metallicity and EW of UV absorption lines. For details we refer to Heckman et al. (1998), and here we briefly summarize the main points:

1. In general, the spectral properties are set by OB stellar populations. The evolutionary history of these correlations strongly depends on the stellar mass loss rates, which in turn depend on the metal abundance (Maeder & Conti 1994).
2. Winds from hot stars contribute to the line profiles of C IV and Si IV. As shown theoretically (and also confirmed observationally), the wind strength of these stars is metal dependent (see Castor et al. 1975; Walborn et al. 1995).
3. Dust extinction is proportional to metallicity and sets the column density for producing the absorption features (e.g., Heckman et al. 1998).
4. Most of the IS lines are optically thick at average column densities of the ISM in star-forming galaxies (e.g., Pettini & Lipman 1995; Heckman et al. 1997; Sahu & Blades 1997). Therefore, their line depths depend only weakly on the column density but more strongly on the velocity dispersion of the absorbing gas.
5. The more metal-rich starbursts are, the more powerful in terms of their UV and IR luminosities. Moreover, they reside in more massive galaxies with higher average ISM velocity dispersion caused by both supernovae and stellar winds. The velocity dispersion widens the optically thick IS lines.

While the relation between EW and metallicity is clearly seen in local galaxies, it has not been verified at higher redshifts. In the following, we combine the data from more than 50 local galaxies and use  $\sim 20$  galaxies at  $z \sim 2$ –3 to test the

<sup>14</sup> Note that different calibrations can lead to up to 0.3 dex different metallicity measurements for single galaxies (e.g., Kewley & Ellison 2008).

relation at high  $z$ . We focus on the strongest lines observed in the spectra of high- $z$  galaxies, which are the photospheric/IS Si III complex at 1300 Å, the IS C II doublet at 1335 Å, and the Si IV and C IV absorption features with IS origin but also affected by stellar winds.

### 2.1. Synthetic Stellar Library Binary Population and Spectral Synthesis (BPASS)

We begin by investigating the relation between absorption line EW and metallicity from a theoretical perspective using a synthetic stellar library created by the BPASS (Eldridge & Stanway 2009, 2012)<sup>15</sup> models. These combine stellar evolution models with libraries of synthetic atmospheric spectra to provide high-resolution modeling of stellar populations. They also include the binary evolution of stars, resulting in stellar populations that are bluer and older than populations of stars without binaries. In addition, the models are postprocessed by Cloudy (Ferland et al. 1998) to include nebular emission. In the following, we use the BPASS models with constant star formation and the contribution of binary stars. Note that these models do not include the IS contribution to the absorption features and therefore only represent their photospheric and wind components. We therefore do not use these models to predict the absolute strengths of absorption features but, instead, investigate their relative dependencies on the underlying age of the stellar population.

We use nine different model populations with different stellar population ages and metallicities. These consist of old (500 Myr), intermediate-age (100 Myr), and young (10 Myr) stellar populations with metallicities of  $Z = 0.001, 0.004,$  and  $0.02$ . In the top five panels of Figure 1, we show the regions around absorption line complexes and He II from BPASS-generated models. The solid, dashed, and dotted lines correspond to old, intermediate-age, and young stellar populations, and the colors show different metallicities. The correlation between IS absorption and metallicity is clearly evident. Also, the models are largely independent of age for stellar populations older than  $\sim 100$  Myr, which indicates that these are good tracers of metallicities for stellar populations above this age threshold. However, for younger ages, the absorption strengths are increased for the C IV and Si IV absorption complex and decreased for Si III. This observation should be kept in mind in the following analysis. Also, the He II emission variations with metallicity are more complicated, so He II is not used in our analysis.

### 2.2. Calibration on Local Galaxies

We consider two partially overlapping samples of local starburst galaxies with UV spectral coverage between 1000 and 2000 Å and measured metallicities from, if available, electron temperature (ratio of [O III] line ratios at different wavelengths) and strong-line methods (using the Edmunds & Pagel (1984) calibration) to investigate the relation between IS absorption line EWs and metallicity. Both samples are based on the *International Ultraviolet Explorer* (IUE) data archives (see Kinney et al. 1993) and are presented in detail in Heckman et al. (1998) and Leitherer et al. (2011). Furthermore, we make sure that these samples do not contain active galactic nuclei (AGNs).

The Heckman et al. (1998) sample consists of a compilation of 45 local starburst galaxies with low-resolution ( $R \sim 200\text{--}300$ ) UV spectral coverage of 1150–2000 Å as well as metallicity measurements from the literature. The metallicity of the sample ranges from  $12 + \log(\text{O}/\text{H}) = 7.5$  to  $12 + \log(\text{O}/\text{H}) = 9.5$ . In their study, Heckman et al. (1998) show the correlation for individual galaxies between metallicity and average IS (Si II, O I, Si III, and C II), as well as IS+wind (C IV and Si IV) absorption EWs. However, since the Si IV and C IV lines show very different EWs, we reextract the spectra from the NED archive<sup>16</sup> and measure the EWs of the lines separately on stacked spectra of different metallicity bins to be consistent with our methods.

The Leitherer et al. (2011) sample consists of a compilation of 46 spectra in subregions of 28 local starburst and star-forming galaxies<sup>17</sup> with moderate-resolution ( $R \sim 1300$ ) UV spectral coverage of 1150–3200 Å as well as metallicity measurements from the literature. The spectra were obtained by the Faint Object Spectrograph (FOS, Harms et al. 1979) as well as the Goddard High Resolution Spectrograph (GHRS, Brandt et al. 1994) on board the *Hubble Space Telescope* (HST). The metallicity of the sample ranges from  $12 + \log(\text{O}/\text{H}) = 7.5$  to  $12 + \log(\text{O}/\text{H}) = 9.5$ . Out of these 46 spectra, we have carefully chosen 22 for which there is good data coverage across the spectral features examined in the previous section and that show no emission due to the O I airglow line at 1304 Å as this would impact the measurement of the Si III absorption complex at 1300 Å. The lower panels of Figure 1 show the stacked spectra in four different metallicity bins in the same five spectral ranges as for the BPASS models. The composites quantitatively show the connection between strong IS absorption and metallicity. Furthermore, the blue wing of C IV is more pronounced for metal-rich systems, in agreement with stellar winds having higher terminal velocities in regions with high metal abundance, as expected from the BPASS models.

Figure 2 shows the correlation between EW and metallicity for the Leitherer et al. (blue circles) and Heckman et al. (green squares) galaxies binned in metallicity. The horizontal error bars represent the dispersion of metallicities in each bin, and the vertical error bars are derived from a Monte Carlo sampling accounting for the uncertainties in the measurements of the continuum. We find a relatively tight, monotonic relation between the EWs and the metallicity, as expected from the BPASS models.

### 2.3. Galaxies at $z \sim 2\text{--}3$

To verify the local relation at higher redshifts, we repeat the previous test at  $z \sim 2\text{--}3$ . First, we use a sample of 20 galaxies at  $2.1 < z < 2.5$  presented in Maier et al. (2014) with zCOSMOS-deep (see Lilly et al. 2007) UV spectra in the observed wavelength range 3600–6800 Å and metallicities estimated by a simultaneous fit (using the Kewley & Dopita (2002) models) to five optical emission lines ([O II], H $\beta$ , [O III], H $\alpha$ , and [N II]) accounting for dust, ionization parameter, and metallicity (see Maier et al. 2005).

For each of these galaxies, we retrieve fully calibrated zCOSMOS-deep UV spectra and measure the EW of the UV absorption features on composite spectra in bins of metallicity,

<sup>15</sup> <http://www.bpass.org.uk>

<sup>16</sup> <http://ned.ipac.caltech.edu/>

<sup>17</sup> <http://www.stsci.edu/science/starburst/templ.html>

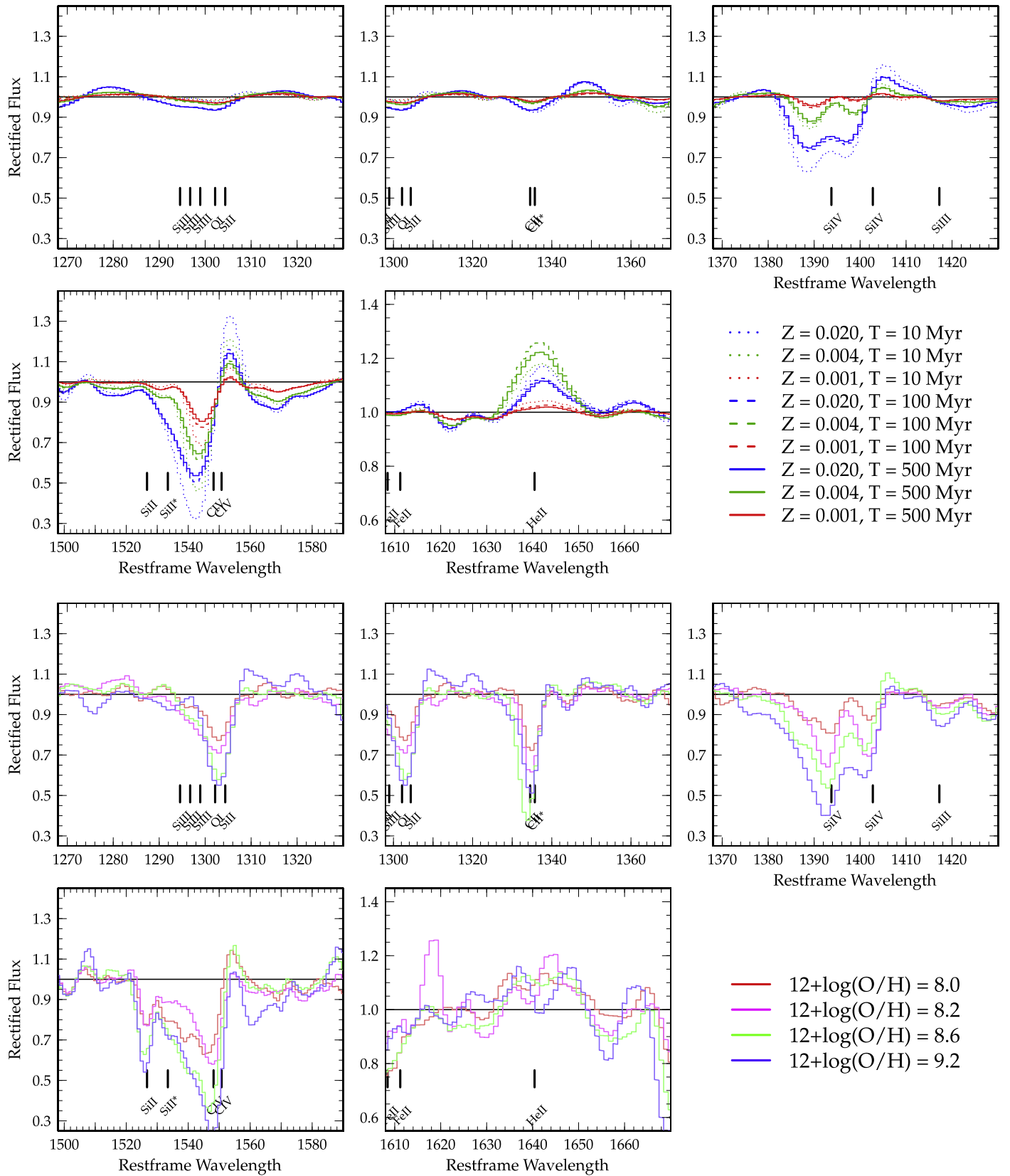


**Figure 1.** Top five panels show absorption-line features as well as He II emission as a function of metallicity and age for synthetic spectra generated by the BPASS code. Shown are models with metallicities  $Z = 0.02$  (blue),  $Z = 0.004$  (green), and  $Z = 0.001$  (red). These metallicity abundances are shown for 10, 100, and 500 Myr old stellar populations, shown in dotted, dashed, and solid lines, respectively. Notice that above  $\sim 100$  Myr there is no significant dependence of the absorption features on age. The bottom five panels show the same wavelength ranges but of 22 observed spectra of local starburst and star-forming galaxies by Leitherer et al. (2011). The spectra are split and stacked in four different metallicity bins given their oxygen abundances measured by various authors (see Leitherer et al. 2011). The general trends of absorption depth with metallicity are consistent with the BPASS models except for the ISM lines that are not included in this model.

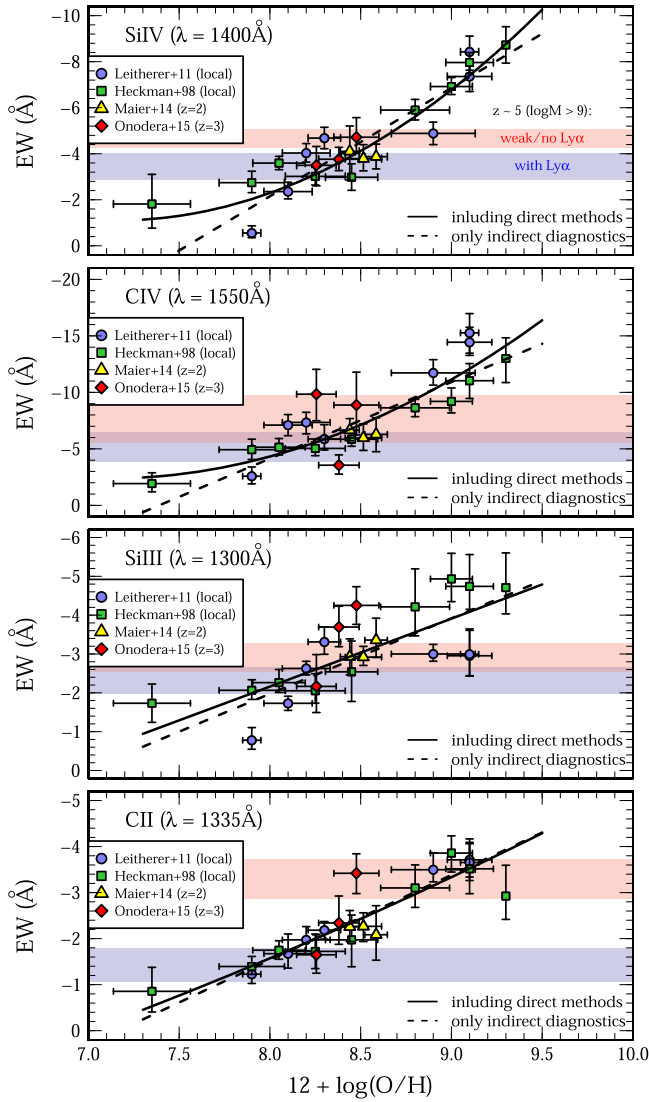


**Figure 2.** Correlation between the rest-frame EW of UV absorption features at 1200–1600 Å and gas-phase metallicity. The symbols show galaxy samples with observed rest-frame UV absorption features and metallicities measured by the strong-line methods. These samples have been compiled at different redshifts and are binned in metallicity: local (blue squares, green circles; Heckman et al. 1998; Leitherer et al. 2011),  $z \sim 2$  (yellow triangles; Maier et al. 2014), and  $z \sim 3$  (red diamonds; Onodera et al. 2016). We verify the locally observed EW versus metallicity relation to hold up to redshift of  $z = 2$ – $3$ . The fitted parameters are given in Table 1, and the fit is shown as a black line (including direct metallicity estimates, solid; only indirect methods, dashed). The bands show ranges of EW for our  $z \sim 5$  galaxies at  $\log(M/M_{\odot}) > 9.0$  with (blue) and without or weak (red)  $\text{Ly}\alpha$  emission.

as will be outlined in the later sections, where we describe the measurements on our  $z \sim 5$  galaxy sample. The result is shown in Figure 2 (yellow triangles). The measurements at  $z \sim 2$  agree well with the local relation between EW and metallicity  $12 + \log(\text{O}/\text{H}) \sim 8.5$ .

A further test is conducted using a sample of 11 galaxies at  $z \sim 3$  with metallicities in the range  $8.0 < 12 + \log(\text{O}/\text{H}) < 8.8$  from Onodera et al. (2016). These galaxies were observed in near-IR using the Multi-object Spectrometer for Infrared Exploration (MOSFIRE; McLean et al. 2012), and metallicities are computed with the Maiolino et al. (2008) calibration using simultaneous strong-line methods, including  $R_{23}$  and line ratios  $[\text{O II}]/[\text{O III}]$ ,  $[\text{O II}]/$

**Table 1**  
Fit to the Relation between EW and Metallicity According to  $\text{EW} = p_0 + p_1 Z + p_2 Z^2$

Absorption	$p_0$	$p_1$	$p_2$
Si III (1300 Å)	$11.371^{+1.918}_{-2.314}$	$-1.621^{+0.503}_{-0.515}$	$-0.007^{+0.029}_{-0.035}$
C II (1335 Å)	$5.479^{+2.027}_{-2.126}$	$-0.102^{+0.487}_{-0.506}$	$-0.098^{+0.028}_{-0.031}$
Si IV (1400 Å)	$-86.288^{+4.209}_{-4.191}$	$23.802^{+0.879}_{-1.071}$	$-1.665^{+0.057}_{-0.056}$
C IV (1550 Å)	$-125.961^{+5.584}_{-5.966}$	$34.797^{+1.304}_{-1.454}$	$-2.449^{+0.078}_{-0.084}$

$\text{H}\beta$ ,  $[\text{O III}]/\text{H}\beta$ , and  $[\text{N III}]/[\text{O II}]$ . The EWs of UV absorption complexes are derived from zCOSMOS-deep UV spectra using the same methods as for the  $z \sim 2$  galaxies. The galaxies (stacked in three metallicity bins by a running mean) are shown with red diamonds in Figure 2. They agree well with the local relation and the  $z \sim 2$  galaxies.

Overall the relation between EW and metallicity appears to hold up to  $z \sim 3$ , a time range of 11 billion years.

#### 2.4. The UV EW versus Metallicity Relation

Since the relation is verified to be valid up to  $z \sim 3$ , we fit this relation for each UV absorption complex by a second-order polynomial function of the metallicity  $Z$  (expressed in  $12 + \log(\text{O}/\text{H})$ ). The fit is valid in the range  $7.3 < 12 + \log(\text{O}/\text{H}) < 9.5$ . The coefficients for each of the UV absorption complexes are given in Table 1, and the best fit is shown in Figure 2 as a solid black line. We estimate the errors on the fit using a Monte Carlo simulation, including the errors on the EW measurements and the widths of the metallicity bins.

While most of the metallicities used for setting up this relation are computed by indirect or strong-line methods (see introduction of this paper), more direct methods (for example via the electron temperature estimated from the ratio of the components of the  $[\text{O III}]$  doublet) are available for local galaxies. However, it has been shown that large discrepancies exist between direct and indirect methods, which could affect our derived relation between UV EWs and metallicity. Direct methods allow us to access and measure low metallicities and therefore provide a leverage of the relation at the low end of metallicity. Removing these direct methods and only focusing on strong-line methods (as they are used for  $z \sim 2$ – $3$  galaxies) does not change the UV EW versus metallicity relation in the range where we expect our high- $z$  galaxies to lie (blue and red bands). This is shown by the dashed black line in Figure 2 and is expected given the large uncertainties that dominate the strong-line methods. Furthermore, we are aware that the metallicities derived using strong-line methods are discrepant by  $\sim 0.2$ – $0.3$  dex, due to the inherent assumptions in these methods (e.g., Kewley & Dopita 2002; Kewley & Ellison 2008). We have propagated this uncertainty through our fitting analysis of the above-quoted relation between UV EW and metallicity.

We now apply this relation to a sample of  $z \sim 5$  galaxies, which we describe in the following section.

### 3. SAMPLE OF $z \sim 5$ GALAXIES

#### 3.1. DEIMOS Campaign on the COSMOS Field

The data are based on the spectroscopic follow-up campaign of the Cosmic Evolution Survey (COSMOS, Scoville et al.

2007) using the DEIMOS (Faber et al. 2003) on the Keck II telescope. This campaign was designed with the goal of building up a sample of high-redshift galaxies that spans a wide range of stellar masses, dust, and galaxy activity in order to study the mass assembly, black hole growth, and feedback processes that control star formation in the early universe. In total, there are about 1500 sources at redshifts  $z > 3.5$ , including galaxies, AGNs, and radio sources. The diverse sample consists of galaxies selected by photometric redshifts, continuum-selected Lyman-break galaxies dropping out in the  $B$ -,  $g$ -,  $V$ -,  $r$ -,  $i$ -, and  $z$ -band broadband filters, narrow-band selected Ly $\alpha$ -emitting galaxies in IA624, NB711, and NB816, and galaxies selected in the infrared as well as radio.<sup>18</sup> For more details on the sample selection, we refer to Mallery et al. (2012).

The observations of the targets were carried out over the course of three years between 2007 January and 2010 February. The DEIMOS setup is a G830 grating blazed at 8640 Å (optimal wavelength range is 5800–9800 Å) with an OG550 blocker and 1" wide slitlets, resulting in a resolution of 3.3 Å (or  $R \sim 2600$ ,  $\delta v = 130 \text{ km s}^{-1}$ ). This is sufficient to distinguish the [O II] $\lambda$ 3727 doublet structure and provides secure redshifts. The average integration time per target is 3.5 hr in blocks of 30 minutes. The raw spectra were reduced and processed by the DEEP2 data-reduction pipeline, which was modified to accommodate dithering. The relative flux calibration was performed by using calibration stars (HZ44, GD71, Feige110) that were observed in the same configurations as the science masks in each individual night, and for the absolute flux calibration we used the existing multiwavelength photometry available on COSMOS.

### 3.2. Sample Selection and Spectroscopic Redshifts

#### 3.2.1. General Sample Selection

The spectroscopic redshifts of the galaxies are determined to first order by their Ly $\alpha$  emission as well as by low- and high-ionization absorption lines (the spectra are analyzed manually by using *SpecPro*; Masters & Capak 2011). The Lyman break detected by broadband photometry is simultaneously used to support the redshifts. A quality flag between 1 (very uncertain redshift) and 4 (very certain redshift) is assigned based on the number of people (three in total) agreeing on the visually estimated redshift. The redshift distribution peaks at  $\langle z \rangle \sim 1.0$  and  $\langle z \rangle \sim 4.5$ . For the purpose of this work, we choose galaxies with  $3.5 < z < 6.0$  (with  $\langle z \rangle \sim 4.8$ ; see Figure 3) in order to have access to their rest-frame UV wavelength range (1200–1800 Å). In an additional step, we manually remove galaxies with (broad) C IV emission at 1550 Å, which indicates a substantial contribution from AGNs (e.g., Allen et al. 1998).

#### 3.2.2. Determination of Redshift

The determination of *systemic* redshifts is difficult at high redshifts, due to strong outflows and resonant scattering of UV spectral features. For our sample of galaxies, the systemic indicators are either blended and too faint to be observed in individual galaxies (photospheric lines Si III, C III, N IV, and

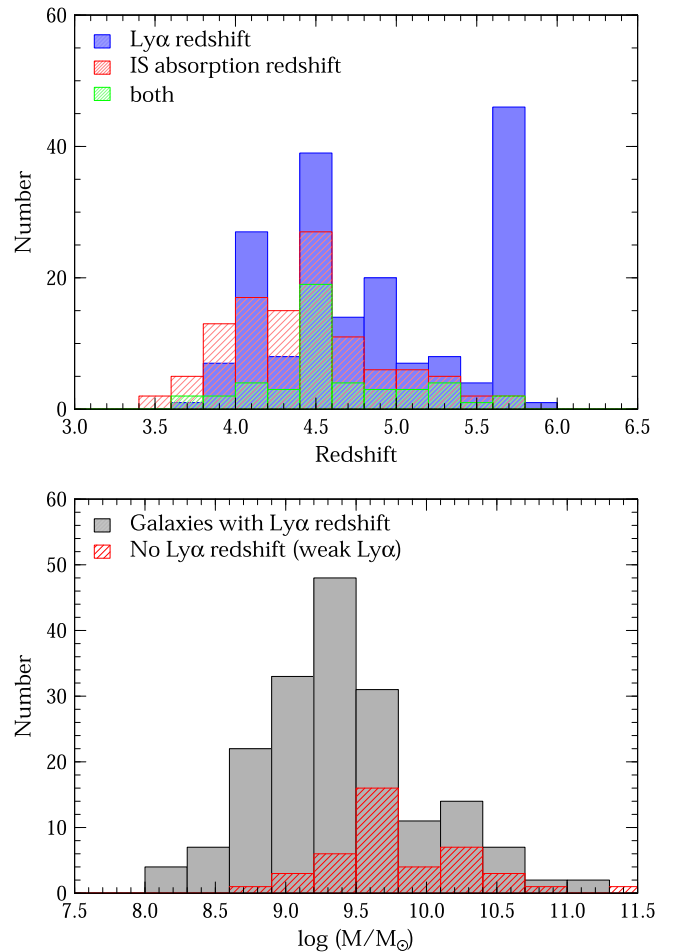


**Figure 3.** Top: redshift distribution for galaxies with Ly $\alpha$  detection; the final sample used this work (blue) measured by fitting a skewed Gaussian to the emission line. The red hatched histogram shows the distribution of redshifts for single galaxies determined from IS absorption features (Si II, C II, Si III, C IV). The green hatched histogram shows galaxies for which redshifts from Ly $\alpha$  and IS absorption features are available. Bottom: the stellar mass distribution of galaxies with Ly $\alpha$  redshifts (gray) and with only weak or no Ly $\alpha$  emission (red). The stellar masses are obtained by SED fitting of 32-band COSMOS photometry including deep *Spitzer*/IRAC photometry (Laigle et al. 2016) to a comprehensive template library using the publicly available code *Le Phare*. The stellar masses are measured for a Chabrier (2003) IMF.

Fe v) or fall out of the wavelength range of ground-based near-IR spectrographs (nebular lines H $\alpha$ , H $\beta$ , and [O III]).

The most prominent spectral features of high- $z$  star-forming galaxies are the Ly $\alpha$  emission, the IS absorption lines (Si II, C II, Si IV, C IV), and the blended photospheric Si II/C III/O I line complex at 1300 Å. The photospheric lines are blended and cannot be used to derive systemic redshifts. The Ly $\alpha$  emission and IS absorption lines are affected by galactic winds and therefore shifted red- and blueward, respectively, by up to 1000 km s $^{-1}$  (e.g., Pettini et al. 2000, 2002; Steidel et al. 2010; Leitherer et al. 2011). These different velocity shifts have to be taken into account when stacking the spectra.

For this work, we aim for a galaxy sample that is as complete as possible in photometric and spectral properties. Thus we include galaxies for which the Ly $\alpha$  line is detected, as well as galaxies that have weak or no Ly $\alpha$  emission or even Ly $\alpha$  in absorption. For the former, the redshifts ( $z_{\text{Ly}\alpha}$ ) are obtained by the fitting of a skewed Gaussian profile to the Ly $\alpha$  emission line, thereby accounting for the absorption on the blue side. For

<sup>18</sup> For the full set of filters available for COSMOS, we refer to Capak et al. (2007) and the official COSMOS web page (<http://cosmos.ipac.caltech.edu/>).

a detailed description of this procedure, we refer to Mallery et al. (2012). The redshifts of the latter ( $z_{\text{IS}}$ ) are measured for individual galaxies from the IS absorption lines as C II, C IV, and Si IV, where the latter two also have a strong wind component. We point out that a careful redshift measurement from the absorption lines by decomposing them into photospheric, IS, and wind components is not possible for single galaxies because of their low signal-to-noise ratio (S/N). This uncertainty in the measured redshift may lead to a broadening of the absorption features in the stacked spectra. We will discuss the impact of this on the measurement of the UV EWs in Section 4.2.2.

The top panel of Figure 3 shows the distribution of Ly $\alpha$  redshifts (blue), the distribution of IS absorption redshifts (red), and the redshift distribution for galaxies for which a redshift from Ly $\alpha$  and IS absorption features is available (green). The spike at  $z \sim 5.7$  contains galaxies selected in narrow-band imaging and therefore strong Ly $\alpha$  emission. We have checked that these galaxies do not bias our sample.

In the following stacking analysis, we will treat these samples (galaxies with and without Ly $\alpha$  emission) separately but will eventually combine them for the measurement of metallicity. This allows us to investigate possible selection effects that would occur if only focusing on one of the two populations. Also, we note that galaxies have in general a diversity of velocity offsets between IS absorption lines and Ly $\alpha$  emission. This complicates the stacking analysis and also affects the quantities measured on the composite spectrum. We will investigate and discuss this later in this paper.

### 3.3. Stellar Masses

#### 3.3.1. The Spectral Energy Distribution Fitting Procedure

The stellar masses for our galaxies are derived from the fitting of COSMOS 32-band photometry from far-UV to IR (including broad and narrow bands in the optical) to a large library of spectral energy distribution (SED) templates at fixed spectroscopic redshifts using the publicly available code `LePhare` (Arnouts et al. 1999; Ilbert et al. 2006; Laigle et al. 2016). In the following, we briefly outline the procedure to obtain stellar masses for our galaxies. For more details on the SED fitting procedure, the imaging data reduction, and the extraction of the photometry, we refer to Laigle et al. (2016) as well as Capak et al. (2007), McCracken et al. (2012), and Ilbert et al. (2010, 2013). The library of synthetic templates is based on Bruzual & Charlot (2003) stellar population synthesis models, assuming a Chabrier (2003) IMF.<sup>19</sup> Star-forming templates include common emission lines ([O II], [O III], H $\alpha$ , H $\beta$ , and Ly $\alpha$ ), which fluxes we define to be proportional to the UV luminosity (Kennicutt 1998). Accounting for emission lines in SED fitting is crucial at  $z \gtrsim 4$  to avoid a systematic overestimation of stellar masses (up to factors of two at  $z \sim 5$ –6), as well as biases in the measurement of colors (e.g., Schaerer & de Barros 2009; Stark et al. 2013; Wilkins et al. 2013; de Barros et al. 2014; González et al. 2014; Santini et al. 2015; Faisst et al. 2016). We use exponentially declining star-formation histories (SFHs) with  $\tau = [0.3, 1, 3, 5, 30]$  Gyr along with delayed models (SFR( $t$ )  $\propto \tau^{-2}e^{-t/\tau}$ ) in which the peak of star formation happens after  $\tau = [0.1, 0.5, 1, 3]$  Gyr.

<sup>19</sup> The conversion of stellar mass to a Salpeter (1955) IMF goes roughly as  $M_{\text{salp}} \sim M_{\text{chab}} \times 1.77$ .

We take into account different metallicities ( $Z_{\odot}$  and  $0.2Z_{\odot}$ ) and vary  $E(B - V)$  between 0 and 0.8. For the extinction curve, we assume the following parameterizations: a  $\lambda^{0.9}$  law (see Arnouts et al. 2013) and a Calzetti et al. (2000) parameterization including a distinct 2175 Å feature that is observed in the extinction curve of the Milky Way and Large Magellanic Cloud as well as in galaxies at  $z = 2$ –4 (e.g., Savage & Mathis 1979; Fitzpatrick 1989; Scoville et al. 2015a). We do not find a significant difference in the stellar mass estimates using the original Calzetti et al. (2000) dust extinction curve. The stellar masses (including active stars and remnants) are defined to be the median of the probability distribution function after marginalizing over the templates. The bottom panel of Figure 3 shows the stellar mass distribution for galaxies with Ly $\alpha$  emission (gray) and with weak or no Ly $\alpha$  emission (red).

The final sample that is used in the following consists of 224 galaxies in the redshift range  $3.5 < z < 6.0$  and stellar masses  $\log(M/M_{\odot}) > 8.0$ . Of these, 182 are detected in Ly $\alpha$  emission, and 42 show weak or no Ly $\alpha$  emission.

#### 3.3.2. Aside: Importance of Mid-IR Photometry at $z > 4$

At redshifts of  $z \gtrsim 3.5$ , the observed optical to near-IR photometry does not cover the 4000 Å Balmer break, which is a sensitive measure of various parameters describing the stellar populations of a galaxy. Therefore, stellar mass estimates at high redshifts that lack mid-IR photometry can be severely biased. To overcome this problem, we use the *Spitzer Large Area Survey with Hyper-Suprime-Cam* (SPLASH; see Steinhart et al. 2014) on COSMOS. The SPLASH provides *Spitzer*/IRAC data at 3.6 and 4.5  $\mu\text{m}$  that are  $\sim 2$  mag deeper ( $> 25.5$  mag at  $3\sigma$  in  $3''$  apertures) than existing mid-IR data on COSMOS and therefore allow us to measure reliable stellar masses at  $z > 4$  by providing a deep coverage of wavelength redder than the 4000 Å break. The *Spitzer* photometry is extracted using an improved version of IRACLEAN (Hsieh et al. 2012) in order to overcome the source confusion (blending) in the *Spitzer* imaging data. For optimal deblending, the combined  $zYJHK_s$  images have been used as a prior for the position and shape of the sources (for more details, see Laigle et al. 2016).

To demonstrate the importance of the mid-IR data, we have performed the stellar mass fitting with and without the addition of mid-IR data from SPLASH. As shown in Figure 4, excluding mid-IR photometry results in an overestimation of the stellar masses at  $\log(M/M_{\odot}) < 10.0$  by up to an order of magnitude at  $z > 3$ . Stellar population ages are overestimated by the same amount. This illustrates that, without constraints in the mid-IR, the SED fitting of these high- $z$  galaxies is dominated by the rest-frame UV part of the SED; that is, it is directly proportional to the UV continuum slope  $\beta$  with no constraints on the 4000 Å break.

## 4. COMPOSITE SPECTRUM OF $z \sim 5$ GALAXIES

In practice, investigations of spectral features as a function of physical parameters (e.g., stellar mass; see below) require us to stack individual galaxy spectra because of the low S/N in individual spectra. In this section, we describe the stacking procedure and the measurements, as well as bias correction of the EWs.

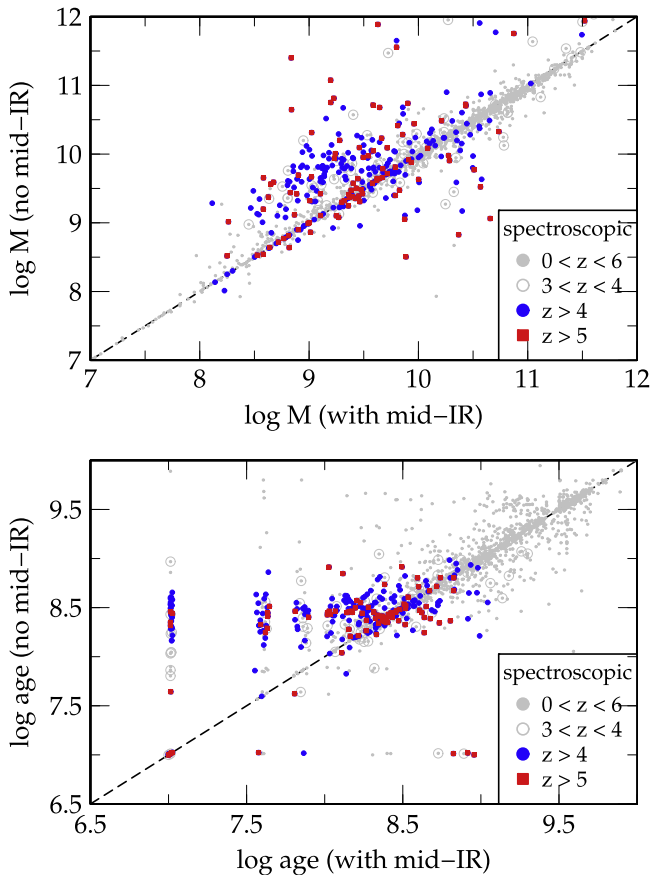


**Figure 4.** Importance of deep mid-IR data for the computation of stellar masses of  $z > 3.5$  galaxies. The two panels show the stellar masses and light-weighted ages of the stellar population from SED fitting including and omitting mid-IR data from *Spitzer*/IRAC. The symbols are colored as a function of spectroscopic redshifts (gray dots:  $0 < z < 6$ ; gray open circles:  $3 < z < 4$ ; blue points:  $z > 4$ ; red squares:  $z > 5$ ). Not using mid-IR data at  $z > 3$  results in overestimated stellar masses by up to one magnitude at  $\log(M/M_{\odot}) < 10.0$  as well as overestimated ages for young galaxies by more than one order of magnitude at  $z \gtrsim 3$ .

#### 4.1. Stacking Procedure

Before stacking, we normalize each individual spectrum to the median flux measured between rest-frame 1250 Å and 1800 Å. Within this wavelength range, we exclude regions of strong absorption lines, including the atmospheric *A* and *B* bands (observed 7600–7630 Å and 6860–6890 Å), the water absorption band (observed  $> 9000$  Å), and the absorption lines Si II (1255–1264 Å), O I/Si II (1290–1307 Å), C II (1326–1340 Å), Si IV (1379–1405 Å), Si II (1521–1529 Å), C IV (1529–1553 Å), Fe II (1600–1613 Å), and Al II (1663–1679 Å). We use the same wavelength windows to fit the continuum, which we use to rectify the individual galaxy spectra before stacking to account for their different UV continuum slopes. The composite spectrum is created by the median stacking of the individual, rectified, and normalized spectra in the rest frame of the Ly $\alpha$  emission line in the case of galaxies detected in Ly $\alpha$  and in the rest frame of IS absorption lines in the case of weak or no Ly $\alpha$  emission. In the former sample (with Ly $\alpha$  emission), the brightest and highest S/N galaxies with strong observed absorption features, however few in number, could bias the derived composite spectrum. We have checked, by removing 12 galaxies fulfilling this criteria, that the inclusion of these does not affect the results of this paper.

The binned and rectified  $\langle z \rangle = 4.8$  composite spectrum in the rest frame of Ly $\alpha$  emission is shown in Figure 5 for galaxies with Ly $\alpha$  emission (black line) and with weak or no Ly $\alpha$  emission (red solid line). For a better comparison of the two stacks, we have shifted the latter into the Ly $\alpha$  rest frame according to the average velocity offset between the Ly $\alpha$  and IS absorption lines measured for individual galaxies (see Appendix). The most prominent spectral features are indicated by vertical lines.

One could argue that the comparison of these two composites is unfair since the stacking in the rest frame of the IS absorption lines may produce more enhanced absorption features than in the case of the composite in the rest frame of Ly $\alpha$  emission. This is because galaxies show a distribution in velocity offsets between the Ly $\alpha$  and IS absorption lines that could blur the spectral features in the case of Ly $\alpha$  stacks. To investigate this effect, we artificially blur the composite spectrum for galaxies with weak or no Ly $\alpha$  emission by shifting the individual spectra randomly according to the Gaussian velocity offset distribution with mean  $\Delta v_{\text{Ly}\alpha\text{-IS}} = 429 \pm 230 \text{ km s}^{-1}$ , as derived in the Appendix. We find that this effect is negligible for the following results. The red dotted line shows one typical realization of this test as an example. The lower panels show a zoom-in on some of the spectral features, including the (blended) Si III/C III/O I complex at 1300 Å, the C II doublet at 1335 Å, the Si IV complex at 1400 Å, the Si II/C IV complex at 1540 Å, the Fe II doublet at 1610 Å, and the He II emission at 1640 Å.

#### 4.2. Equivalent Widths

##### 4.2.1. Measurement

The rest-frame EW of absorption features characterizes the physical properties of galaxies. In this section, we measure EWs of different spectral features that we will later use to quantify the metal content of our galaxies.

The EW of a spectral features is defined as

$$\text{EW} \equiv \int_{\lambda} \left( 1 - \frac{f_{\lambda, \text{feat}}}{f_{\lambda, \text{cont}}} \right) d\lambda, \quad (1)$$

where  $f_{\lambda, \text{feat}}$  is the flux density across the absorption/emission feature, and  $f_{\lambda, \text{cont}}$  is the flux density of the continuum (both in  $\text{erg s}^{-1} \text{cm}^2 \text{Å}^{-1}$ ). Here, we define a “pseudocontinuum” across the spectral feature by a linear interpolation of the median continuum measured red- and blueward in a 10–20 Å window. In the case of absorption lines, we integrate over the pixels below this pseudocontinuum and vice versa for emission lines. We find that the measurement of the pseudocontinuum is the major source of uncertainty. This is especially true for galaxies at high redshifts and low S/N, and we therefore estimate the uncertainties of the measured EW by Monte Carlo’ing over different pseudocontinua, which are obtained including the errors in their flux densities.

##### 4.2.2. Uncertainties, Biases, and Limitations

There are several biases and uncertainties in the measurements of the EWs. First, individual galaxies show different velocity offsets of absorption lines with respect to their systemic redshift. Stacking them in the rest frame of the Ly $\alpha$  emission line may cause a broadening of these absorption

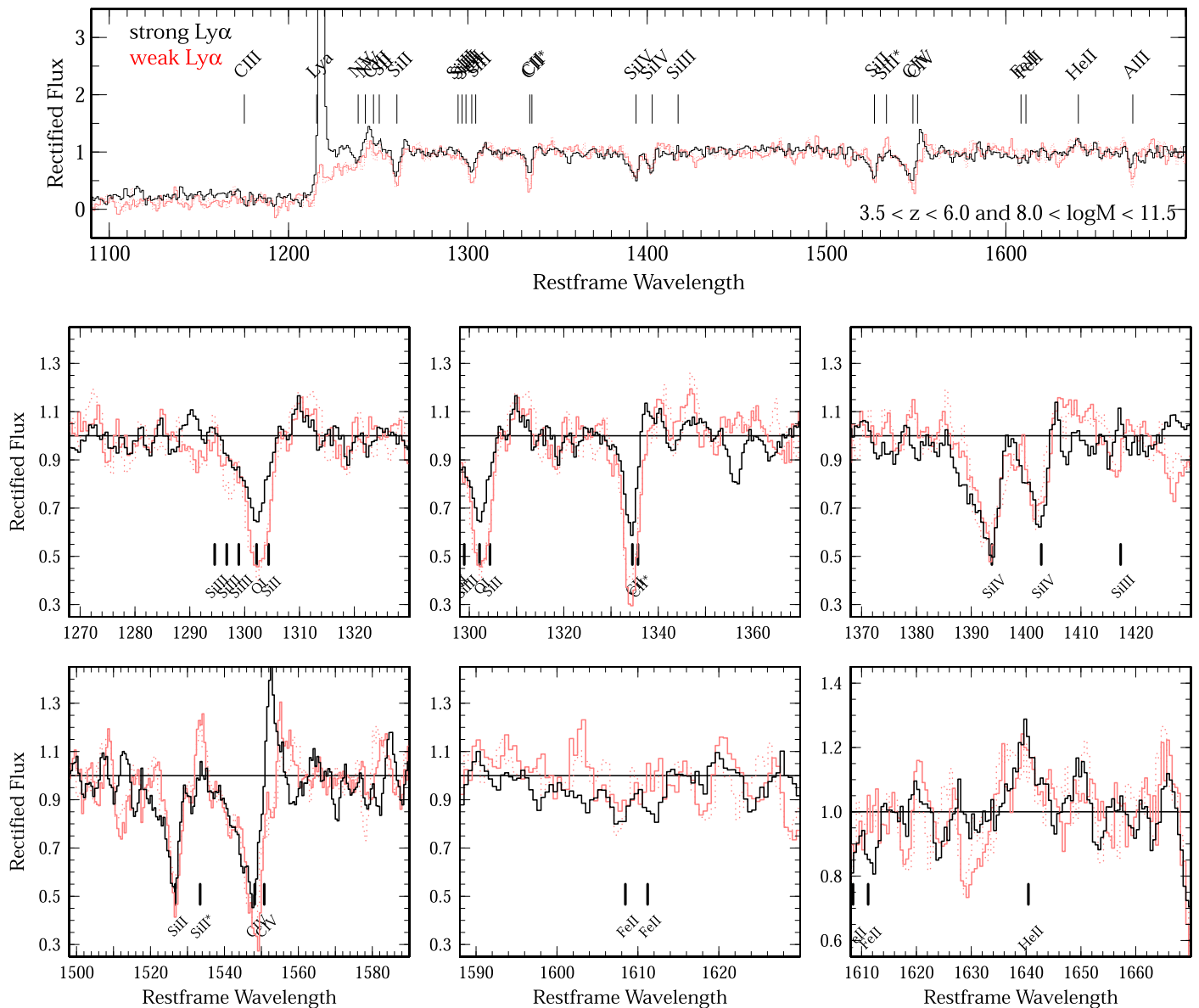


**Figure 5.** Continuum-normalized composite spectrum for all galaxies at  $3.5 < z < 6.0$  ( $\langle z \rangle = 4.8$ ) and  $8.0 < \log(M/M_{\odot}) < 11.5$  (top) and zoom-in on the most prominent absorption complexes as well as He II (bottom). The black lines show galaxies with Ly $\alpha$  emission. The solid red lines show the composite spectrum of galaxies with weak or no Ly $\alpha$  emission, indicating their deeper absorption. The dashed red lines show the latter composite blurred with the average velocity dispersion  $\Delta v_{\text{Ly}\alpha-\text{IS}} = 429 \pm 230 \text{ km s}^{-1}$ . The vertical lines name prominent absorption and emission features, and the horizontal line on the zoom-in shows the continuum.

features. Second, there are uncertainties in the measurement of low EWs introduced by background noise. The latter does also set a detection limit.

We first investigate the effect of velocity offsets on the measured EW. For this we create 100 representations of a composite spectrum by shifting each individual spectrum according to the probability distribution of the velocity offsets derived in the Appendix and listed in Table 3. For each representation, we measure the EW of the absorption features and compute the  $1\sigma$  dispersion (see Table 2). We find the corresponding error on the EW measurements to be less than 20%. This is smaller than or similar to the measurement uncertainties of the EWs and is therefore not a dominant source of error.

Next, we investigate possible biases in the measurement of the EWs that are due to the effect of background noise. We create artificial composite spectra with Gaussian absorption

**Table 2**  
Dispersion in EW Measurements Due to Variations in Velocity Offsets between Ly $\alpha$  and IS Absorption Features Estimated from 100 Monte Carlo Runs

Absorption feature	Dispersion in EW ( $1\sigma$ , in $\text{\AA}$ ) for Velocity-offset Dispersion of $230 \text{ km s}^{-1}$
Si IV	0.32
C IV	0.53
Si III	0.18
C II	0.10

features (placed at  $1330 \text{ \AA}$ ) for a grid of input EWs and include a noise level that we measure on the real composite spectra. We systematically underestimate absorption EWs stronger than  $1.5 \text{ \AA}$  by  $\sim 5\%$ . EWs weaker than  $1 \text{ \AA}$  are still detected but

**Table 3**  
List of Prominent Absorption Features

Line Properties				Measured on Composite $z \sim 5$ Spectrum <sup>a</sup>			
Feature	$\lambda_{\text{vac}}$ (Å)	$E_{\text{ion}}$ (eV)	Environment <sup>b</sup>	$\lambda_{\text{Ly}\alpha}$ (Å) <sup>c</sup>	$\Delta v_{\text{Ly}\alpha-\text{IS}}$ <sup>d</sup>	$\Delta v_{\text{sys}}$ <sup>e</sup>	EW <sub>rest</sub> (Å) <sup>f</sup>
Emission Lines							
Ly $\alpha$	1215.67	–	IS	1216.0	0	300 (340) $\pm$ 170	–
He II	1640.00	–	neb	1638.0 $\pm$ 0.5	–370	–70 (20) $\pm$ 230	1.7 $^{+1.1}_{-0.7}$
Si III Absorption Complex: 1290–1310 Å							
Si III	1294.54	16.35	photo	– <sup>g</sup>	– <sup>g</sup>	– <sup>g</sup>	– <sup>g</sup>
C III	1296.33	24.38	photo	– <sup>g</sup>	– <sup>g</sup>	– <sup>g</sup>	– <sup>g</sup>
Si III	1296.74	16.35	photo	– <sup>g</sup>	– <sup>g</sup>	– <sup>g</sup>	– <sup>g</sup>
Si III	1298.93	16.35	photo	– <sup>g</sup>	– <sup>g</sup>	– <sup>g</sup>	– <sup>g</sup>
O I	1302.17	0.00	IS	1301.0 $\pm$ 0.5	–300	0	– <sup>g</sup>
Si II	1304.37	8.15	IS	– <sup>g</sup>	– <sup>g</sup>	– <sup>g</sup>	– <sup>g</sup>
for this complex							–2.2 $^{+0.4}_{-0.4}$
C II Absorption Complex: 1330–1340 Å							
C II	1334.53	11.26	IS	1332.0 $\pm$ 0.5	–570	–270 (–180) $\pm$ 230	– <sup>g</sup>
C II <sup>a</sup>	1335.71	11.26	IS	1333.0 $\pm$ 0.5	–610	–310 (–220) $\pm$ 230	– <sup>g</sup>
for this complex							–1.6 $^{+0.3}_{-0.3}$
Si IV Absorption Complex: 1385–1410 Å							
Si IV	1393.76	33.49	IS, wind	1391.0 $\pm$ 0.5	–590	–290 (–200) $\pm$ 230	–
Si IV	1402.77	33.49	IS, wind	1401.0 $\pm$ 0.5	–590	–290 (–200) $\pm$ 230	–
for this complex							–4.1 $^{+0.4}_{-0.4}$
C IV Absorption Complex: 1520–1555 Å							
Si II	1526.71	8.15	IS	1524.0 $\pm$ 0.5	–530	–230 (–140) $\pm$ 230	– <sup>g</sup>
Fe IV	1530.04	30.65	photo	1529.0 $\pm$ 0.5	–200	100 (190) $\pm$ 230	– <sup>g</sup>
Si II <sup>a</sup>	1533.43	8.15	IS	–	–	–	–
C IV	1548.19	47.89	IS, wind	1543.0 $\pm$ 0.5	–1010	–710 (–620) $\pm$ 230	– <sup>g</sup>
C IV	1550.77	47.89	IS, wind	1546.0 $\pm$ 0.5	–920	–620 (–530) $\pm$ 230	– <sup>g</sup>
for this complex							–6.4 $^{+1.3}_{-1.4}$
Fe II Absorption Complex: 1600–1620 Å							
Fe II	1608.45	7.87	IS	1606 $\pm$ 0.5	–460	–160 (–70) $\pm$ 230	– <sup>g</sup>
Fe II	1611.20	7.97	IS	1610 $\pm$ 0.5	–230	70 (160) $\pm$ 230	– <sup>g</sup>

**Notes.** See also Leitherer et al. (2011) and references therein.

<sup>a</sup> Galaxies with  $3.5 < z < 6.0$  and  $\log(M/M_{\odot}) > 8.0$ .

<sup>b</sup> Photospheric (photo), interstellar (IS), in winds of massive stars (wind), nebular (neb).

<sup>c</sup> On the stacked spectrum in the rest frame of Ly $\alpha$ .

<sup>d</sup> With respect to Ly $\alpha$  in km s<sup>–1</sup>. The errors are on the order of  $\pm 100$  km s<sup>–1</sup>.

<sup>e</sup> With respect to systemic redshift calibrated by O I in km s<sup>–1</sup>. Values corrected for biases introduced by stacking (see the text) are given in brackets.

<sup>f</sup> Bias corrected, see text.

<sup>g</sup> Line is blended, and no reliable wavelength, velocity offset, or EW can be measured in this case.

with a more substantial overestimation of up to  $\sim 30\%$  on average. Although these biases are small compared to the uncertainties in the measurements, we correct for these in the following.

In Table 3 we list the (corrected) rest-frame EW measured on the composite spectrum of  $\log(M/M_{\odot}) > 8$  galaxies for five different absorption complexes (Si III (1300 Å), C II (1335 Å), Si IV (1400 Å), C IV (1550 Å), and Fe II (1610 Å)) as well as He II. Note that the uncertainty on the latter (only observable in the highest redshift galaxies) is large because of the decreasing number of galaxies and S/N of the spectra at high redshifts.

## 5. RESULTS

### 5.1. Dependences on EW

Relations between metallicity (i.e., UV absorption EW) and dust, SFR, and stellar mass are expected from galaxies at lower redshifts ( $z < 2$ ). In the following, we focus on the dependence of UV absorption EWs on SFR and dust attenuation.

We derive the line-of-sight dust attenuation for our galaxies from the UV continuum slope  $\beta$  ( $\log(f_{\lambda}) \sim \beta \log(\lambda)$ ), which is fit on the COSMOS broadband photometry between rest-frame 1300 and 2200 Å. We restrict our sample to galaxies for which at least four filters are available for the fitting of  $\beta$ . The SFRs

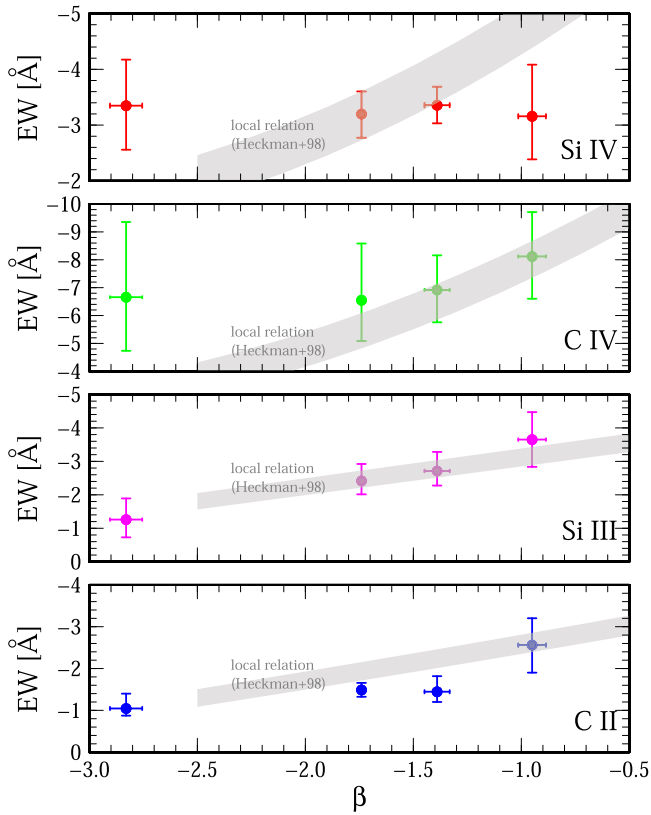


**Figure 6.** Dependence of EW of UV absorption complexes on UV continuum slope  $\beta$  (dust attenuation) measured from COSMOS broadband photometry between 1300 and 2200 Å. The points show our measurements at  $z \sim 5$ , and the gray bands show the relation measured for local galaxies (Heckman et al. 1998). Both data agree well within the measurement uncertainties for  $\beta > -2$  (except for Si IV and C IV, which might be due to their strong wind components). This indicates a correlation between dust and metal content in  $z \sim 5$  galaxies similar to what is seen in local galaxies.

are derived from SED fitting and do not include (rest-frame) far-IR data and should therefore be taken with caution.

Figure 6 shows the dependence between EW and line-of-sight dust for our four different absorption complexes (points), along with the relation between EW and  $\beta$  from local galaxies (gray bands; Heckman et al. 1998) derived by inverting our relation between EW and metallicity (see Section 2). We do not find a significant correlation between these quantities; however, within the uncertainties of our measurements, we find a good agreement with the expected local trends, except for Si IV and C IV. This might be due to the strong wind over the IS component in these lines. This finding shows the similar behavior of dust versus metallicity between local and high- $z$  galaxies.

Figure 7 shows the dependence of EW on the SFR of our high- $z$  galaxies (points) along with the measurements from  $z = 0-2.2$  galaxies in the same stellar mass range derived by inverting the relation between EW and metallicity (gray bands; Mannucci et al. 2010). Within the uncertainties of our measurements, we find again a good overall agreement between the trends in our high- $z$  sample and that of low- $z$  galaxies. A trend of galaxies with higher SFRs showing lower metallicity is expected in a picture where SFR is held up and fueled by the inflow of pristine (i.e., metal-poor) gas (see also Lilly et al. 2013; Feldmann 2015). Furthermore, metals can be

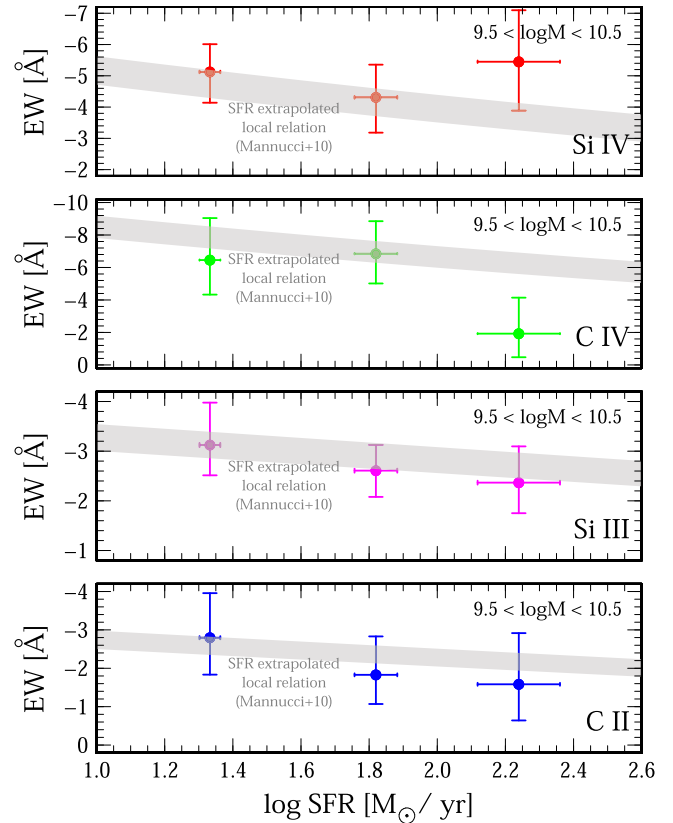


**Figure 7.** Dependence of EW of UV absorption complexes on star formation (measured from SED fitting). The points show our measurements at  $z \sim 5$ , and the gray bands show the relation between metallicity and star formation for  $z = 0-2.2$  galaxies based on emission lines (Mannucci et al. 2010). We have converted the metallicity to UV EW by using our relations presented in Table 1. Within the measurement uncertainties, we find a similar trend between EW and SFR as in local galaxies. Assuming EW as a tracer for metallicity, this trend is expected in a picture where star formation is held up by an inflow of pristine (i.e., metal-poor) gas.

expelled from (low-mass) galaxies by strong outflows, due to their high star-formation rate.

In summary, the trends between the EW of UV absorption lines and  $\beta$  and SFR are weak and of low significance in our  $z \sim 5$  sample. Larger samples and more accurate measurements of SFRs are necessary to improve these results. However, our measurements show a good overall agreement with the trends expected from lower-redshift galaxies within the measurement uncertainties.

## 5.2. Metallicity versus Stellar Mass at $z \sim 5$

We now investigate the dependence of UV absorption EW on stellar mass. For this, we split the sample of our 224 galaxies into three bins of stellar mass:  $8.5 < \log(M/M_\odot) < 9.0$ ,  $9.0 < \log(M/M_\odot) < 10.0$ , and  $\log(M/M_\odot) > 10.0$ . We designed these bins to maximize the S/N as well as the baseline in stellar mass, but a different binning does not change our results.

In Figure 8 (see also Table 4), we show the UV absorption EWs as a function of stellar mass for each of the four absorption complexes. We split galaxies with Ly $\alpha$  emission and weak or no Ly $\alpha$  emission (only shown for  $\log(M/M_\odot) > 9$  because of their small number). While for  $\log(M/M_\odot) < 9$  galaxies the Si IV and C II are in good

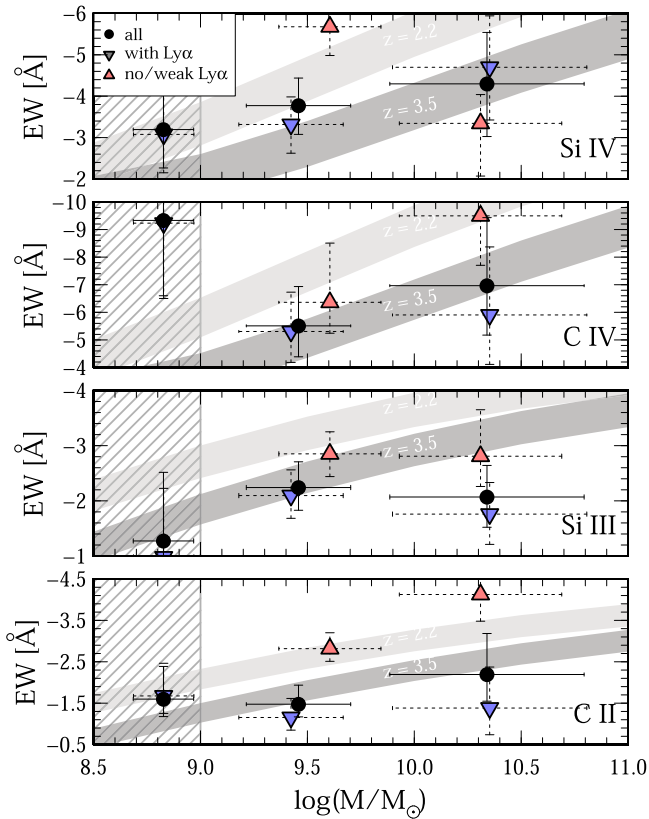


**Figure 8.** Dependence of EW of UV absorption complexes on stellar mass. The points show our data at  $z \sim 5$  (black dots). We split galaxies with Ly $\alpha$  emission (blue down-triangles) and weak/no Ly $\alpha$  emission (red up-triangles, only shown for  $\log(M/M_{\odot}) > 9$  because of their small number). The gray bands show the expected correlation from the relations between mass and metallicity at  $z = 2.2$  and  $z = 3.5$  from the literature. We have converted the metallicity to UV EW by using our relations presented in Table 1. The data in the hatched region ( $\log(M/M_{\odot}) < 9$ ) depend significantly on age, especially in the case of C IV and Si III (see text), and are therefore not considered here. At a fixed stellar mass,  $z \sim 5$  with Ly $\alpha$ -emission galaxies show systematically  $>1\sigma$  lower UV EWs than  $z = 2.2$  galaxies but similar values to  $z = 3.5$  galaxies. Galaxies with weak or no Ly $\alpha$  emission show enhanced EWs similar to  $z \sim 2.2$  galaxies.

agreement with the expectation of an increasing EW with stellar mass, C IV shows an excess and Si III a deficit in EW. This discrepancy could be explained by two reasons: the lower S/N of the low-mass galaxies and their young ages predominantly  $<100$  Myr (also verified by the stellar population ages estimated from SED fitting). As described in Section 4.2.2, we correct for the former, and therefore this effect cannot explain the discrepancies. The latter is expected to have a dominant impact on the UV EWs. As shown by the BPASS models (see Figure 1), galaxies younger than  $\sim 100$  Myr show an excess in C IV and a deficit in Si III compared to older stellar populations at all metallicities. Unfortunately, this trend cannot be verified by the samples used to calibrate the EW versus metallicity relation since these galaxies are not representative of these young stellar populations.

Focusing on  $\log(M/M_{\odot}) > 9$ , we find no significant trend of higher UV EWs for more massive galaxies in all of the absorption complexes, but there are differences in the normalization. Note that we do not expect all absorption complexes to show the same behavior. This is because these elements are produced in different regions of the galaxy. For example, Si III

may be produced at lower temperature and deeper in the ISM compared to C IV or Si IV. The expected relations between EW and stellar mass for  $z = 2.2$  and  $z = 3.5$  galaxies derived by inverting our EW versus metallicity relation are shown as light and dark gray bands. The error bars indicate the 90% percentile scatter for the measurements of the EW including measurement errors and modeling uncertainties. For Ly $\alpha$ -emitting galaxies, the EWs are comparable to the ones expected for  $z = 3$ – $3.5$  galaxies, but, as mentioned above, there is no significant EW versus stellar mass relation for our  $z = 5$  galaxies. Galaxies with weak or no Ly $\alpha$  emission are systematically offset to larger UV EWs at a fixed stellar mass compared to galaxies with Ly $\alpha$  emission (see also the next section for a more qualitative statement). This, yet weak, offset is also seen in their resulting metallicity estimates, as shown below.

Next, we convert these UV EWs into metallicities. For a given EW, we compute its corresponding metallicity by a  $\chi^2$  minimization to the second-order polynomial fit derived in Section 2. The errors are estimated by a Monte Carlo sampling that accounts for the uncertainty of the EW measurements as well as the input EW versus metallicity relation. This is done for each single absorption complex. We then compute a combined metallicity for all the absorption complexes by the weighted mean of the normalized probability distribution function derived from the single absorption complexes. The weights are determined from the covariance matrices of the corresponding EW versus metallicity relations. The results are listed in Table 4. The symbols in Figure 9 show our results (for galaxies with and without Ly $\alpha$  emission) for the combined absorption complexes along with measurements from the literature at  $z = 0.07$  (Kewley & Ellison 2008),  $z = 0.7, 2.2, 3.5$  (Maiolino et al. 2008), and  $z = 3.0$  (Mannucci et al. 2009) including scatter. The errors on the points (90% percentiles) include systematic uncertainties (from the measurement of the EW and the EW versus metallicity relation) as well as the scatter in the metallicity measurements from single absorption complexes. The data reflect our previous results that (1) the metal content of  $z = 5$  Ly $\alpha$ -emitting galaxies is similar to  $z \sim 3$ – $3.5$  galaxies ( $\sim 0.3$  dex lower than at  $z \sim 2$ ) and (2) galaxies with weak or no Ly $\alpha$  emission show slightly higher average metallicities comparable to  $z \sim 2$  galaxies. The MZ relation of the average population of  $z \sim 5$  galaxies is found to be very weak but similar to what is found at  $z \sim 3.5$ , including the uncertainties in our method. Note that our findings are in line with Ando et al. (2007), who measured a metallicity of  $12 + \log(\text{O}/\text{H}) = 8.0$  at  $z = 5$  and  $\log(M/M_{\text{sun}}) = 10.8$  using a similar method as here.

Summarizing, we find a more than a factor of two lower metal content for the average population of  $z = 5$  Ly $\alpha$ -emitting galaxies compared to  $z = 2$ . Including all the scatter in the data, this result is of  $<2\sigma$  significance. The metallicities are comparable to  $z = 3$ – $3.5$  galaxies, and we find no significant MZ relation within our estimated uncertainties. We find an enhanced metal content of weak-Ly $\alpha$ -emitting galaxies on average at all masses compared to strong-Ly $\alpha$ -emitting galaxies.

### 5.3. Ly $\alpha$ versus Weak or No Ly $\alpha$ Emission

We have designed our sample to be as complete as possible, so it includes galaxies with strong Ly $\alpha$  emission as well as galaxies with weak or no emission. In the following, we investigate the properties of these two populations in more

**Table 4**  
Bias-corrected Rest-frame EW Measurements and Estimated Metallicities for  $z \sim 5$  Galaxies Split in Different Stellar Mass Bins

$\log(M/M_{\odot})$	# Galaxies <sup>a</sup>	EW ( $\text{\AA}$ )				$12 + \log(\text{O}/\text{H})$				
		Si IV	C IV	Si III	C II	Si IV	C IV	Si III	C II	All <sup>b</sup>
>8.0	224 (42)	$-4.09^{+0.35}_{-0.45}$	$-6.37^{+1.26}_{-1.35}$	$-2.20^{+0.33}_{-0.42}$	$-1.63^{+0.23}_{-0.28}$	$8.45^{+0.13}_{-0.16}$	$8.31^{+0.28}_{-0.47}$	$8.06^{+0.35}_{-0.32}$	$8.01^{+0.21}_{-0.26}$	$8.30^{+0.26}_{-0.32}$
>9.0	178 (40)	$-3.71^{+0.55}_{-0.60}$	$-5.54^{+1.09}_{-1.46}$	$-2.42^{+0.31}_{-0.36}$	$-1.82^{+0.36}_{-0.37}$	$8.35^{+0.18}_{-0.28}$	$8.10^{+0.39}_{-0.29}$	$8.17^{+0.35}_{-0.35}$	$8.07^{+0.25}_{-0.37}$	$8.26^{+0.31}_{-0.51}$
8.5–9.0	41 (2)	$-3.19^{+0.93}_{-0.99}$	$-9.33^{+2.73}_{-3.05}$	$-1.27^{+0.67}_{-1.24}$	$-1.60^{+0.42}_{-0.79}$	$8.09^{+0.45}_{-0.73}$	$8.43^{+0.25}_{-1.08}$	$7.54^{+0.85}_{-0.45}$	$7.99^{+0.48}_{-0.53}$	$8.05^{+0.56}_{-0.74}$
9.0–10.0	135 (27)	$-3.77^{+0.69}_{-0.67}$	$-5.51^{+1.12}_{-1.42}$	$-2.24^{+0.41}_{-0.47}$	$-1.48^{+0.31}_{-0.46}$	$8.31^{+0.24}_{-0.52}$	$8.14^{+0.37}_{-0.71}$	$8.09^{+0.39}_{-0.42}$	$7.91^{+0.29}_{-0.33}$	$8.12^{+0.33}_{-0.52}$
>10.0	43 (13)	$-4.30^{+1.27}_{-1.24}$	$-6.97^{+1.79}_{-2.46}$	$-2.07^{+0.55}_{-0.57}$	$-2.19^{+0.64}_{-0.99}$	$8.37^{+0.27}_{-0.70}$	$8.24^{+0.41}_{-1.02}$	$7.96^{+0.42}_{-0.52}$	$8.13^{+0.46}_{-0.60}$	$8.32^{+0.40}_{-0.74}$

### Notes.

<sup>a</sup> Total number of galaxies. The numbers in brackets count galaxies with weak or no Ly $\alpha$  emission.

<sup>b</sup> Simultaneous fit to all absorption complexes.

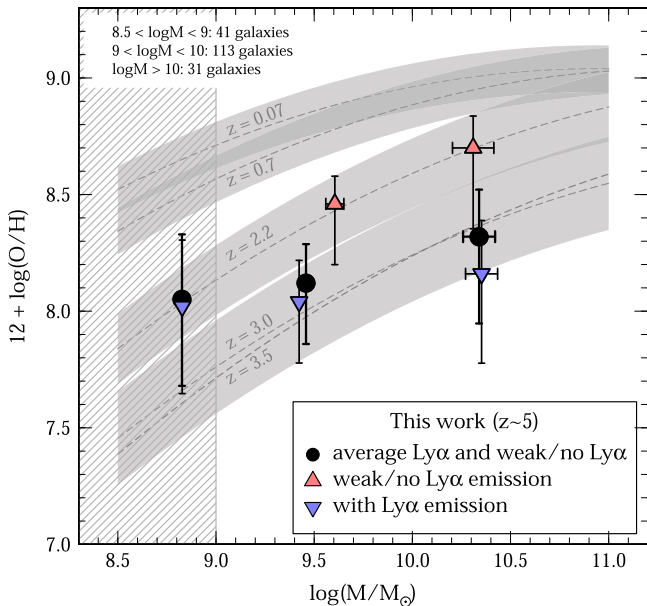


**Figure 9.** Gas-phase metallicity as a function of stellar mass for galaxies at different redshifts. The large symbols show our results at  $z \sim 5$  split in galaxies with Ly $\alpha$  emission (blue), weak or no Ly $\alpha$  emission (red), and the average of both (black). The metallicities are obtained by a simultaneous fit to all the absorption complexes (see text). The dashed lines show different measurements from the literature at  $z = 0.07$  (Kewley & Ellison 2008),  $z = 0.7$ , 2.2, 3.5 (Maiolino et al. 2008), and  $z = 3.0$  (Mannucci et al. 2009) including scatter. Ly $\alpha$ -emitting galaxies at  $z \sim 5$  have a metal content similar to  $z \sim 3$ –3.5 galaxies and only a weak dependence on stellar mass. Galaxies devoid of Ly $\alpha$  emission show a higher metallicity at fixed mass comparable to  $z \sim 2$  galaxies together with a stronger dependence on stellar mass. This is indicative of them being more evolved systems and highlights the diversity among  $z \sim 5$  galaxies.

detail. Figure 9 shows the MZ relation split in galaxies with Ly $\alpha$  emission (blue) and with weak or no emission (red). The latter is only shown at  $\log(M/M_{\odot}) > 9$  because of the lack of a sufficient number of galaxies in the lowest-mass bin. At a fixed stellar mass, galaxies with weak or no Ly $\alpha$  emission show a more than a factor of two higher metal content than galaxies with strong Ly $\alpha$  emission at  $z \sim 5$ . In particular, their metal content is similar to that found in  $z = 2$  galaxies. Including all possible measurement and model uncertainties, we estimate the significance of this result to be low, and we therefore carry out more detailed investigations. Because of the large uncertainties stemming from the mapping of EW to metallicity, it is advantageous, for the assessment of the true statistical significance, to go back to the actual measurements, that is, the difference of EWs for the two populations (see Figure 8).

We investigate the combined significance at a fixed stellar mass bin using a  $\chi^2$  test. We find the  $p$  values to be 0.24 and 0.03 for  $\log(M/M_{\odot}) = 9.5$  and  $\log(M/M_{\odot}) = 10.5$ , respectively. The same analysis in metallicity space yields a  $p$  value of 0.16 for a difference simultaneously in both stellar mass bins. Taking these values at face value, we do not claim a statistically significant difference at low masses between the two populations of galaxies, while the combined offset at high masses is statistically more significant. The general trend of this result (weak-Ly $\alpha$ -emitting galaxies having higher metal content) would not be surprising. Since Ly $\alpha$  is resonantly scattered on neutral gas in the galaxy, which is in turn correlated with dust, a weak Ly $\alpha$  emission would occur in a dusty system, in agreement with having a higher average metal content. In summary, these results, although only significant at high masses, are consistent with a picture in which weak-Ly $\alpha$ -emitting galaxies are more evolved with higher dust and metal content. This result is strengthened by the observation of a less-prominent P-Cygni profile in these galaxies (see Figure 5).

## 6. WHAT WOULD WE EXPECT THE MZ RELATION TO BE AT HIGH $z$ ?

Up to redshifts of  $z \sim 3$ , a strong dependence of metallicity on stellar mass is measured. This indicates the gradual build-up of stellar mass and metallicity over time including feedback, gas inflows, and gas outflows. Furthermore, metallicity is directly linked to the gas and dust content of galaxies (e.g., Roseboom et al. 2012; Feldmann 2015), inducing a relation between stellar mass and dust attenuation (e.g., Garn & Best 2010; Finkelstein et al. 2012; Sobral et al. 2012; Heinis et al. 2014; Oteo 2014; Santini et al. 2014). Also, it is expected that a negative correlation exists between SFR and metallicity, which might be due to feedback or star formation fueled by the accretion of pristine gas onto the galaxy (e.g., Mannucci et al. 2010). Galaxies at low  $z$  have formed over several billion years and thus had time to reach an equilibrium state between the above quantities and to set up the observed relations. Several studies have shown that these relations hold up to redshifts as high as  $z = 3$ –3.5. A correlation between stellar mass and dust is even expected up to  $z = 7$  (e.g., Finkelstein et al. 2012), although the stellar mass estimates in these studies are very uncertain, due to the lack of deep observed mid-IR data.

Taking these local relations directly at face value and applying them to higher redshifts, we would thus expect positive correlations between metallicity (i.e., UV absorption line EW), stellar mass, and dust extinction, as well as a negative correlation between metallicity and SFR. Indeed, our

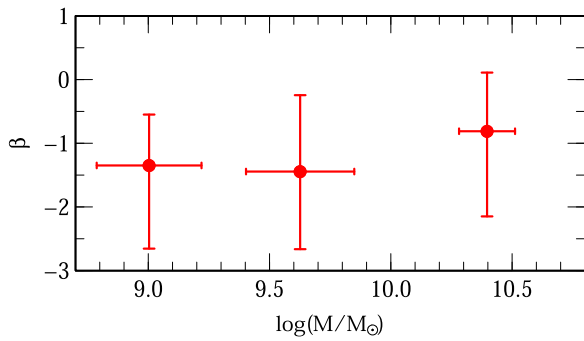


**Figure 10.** Dependence of UV continuum (dust attenuation) on stellar mass for our  $z \sim 5$  galaxies. We do not find a significant correlation between dust and stellar mass, in contradiction to studies at lower redshifts.

data show a weak dependence between dust attenuation and UV absorption EW similar to what is found for local galaxies, indicating that the dust versus metallicity relation is intact at  $z = 5$  (Figure 6). Furthermore, we see hints of a negative trend between SFR and UV absorption strength, again similar in amplitude to what would be expected from low- $z$  data. Such a trend, if true and verified by larger data samples, is indicative of strong accretion of pristine gas in high- $z$  galaxies as fuel for their star formation (Figure 7). However, we do not see a significant correlation between stellar mass and dust attenuation (Figure 10) for the average galaxy population, so it is not unexpected that we do not see a significant correlation between stellar mass and metallicity either (Figure 9). This indicates that something might be changing at  $z \sim 5$  and local relations are starting to weaken.

What could be the cause for a weak or no relation between stellar mass and metallicity at  $z = 5$ ? It might be that our assumption and observational techniques fail at these redshifts. First, galaxies at high  $z$  are dominated by emission lines that can substantially boost their stellar masses (e.g., Schaerer & de Barros 2009; Atek et al. 2011; Stark et al. 2013; Faisst et al. 2016). Although we include emission lines in our SED templates, their contribution and strength are not known reliably, and the obtained stellar masses can still be biased (see, e.g., Hsu et al. 2014). This effect would in particular boost the masses of low-mass galaxies with significant [O III] emission (Atek et al. 2011). Second, there are indications that the strong-line methods (used to calibrate our relation between UV absorption line and metallicity up to  $z = 3$ ) are less reliable at high  $z$  due to the changing internal properties of the galaxies (Masters et al. 2014; Steidel et al. 2014; Sanders et al. 2015a; Shapley et al. 2015). Finally, going hand in hand with the previous point, the relation between EW and metallicity may not be applicable at  $z > 3$ . In fact, the internal properties and structure of very-high-redshift galaxies is not fully understood and could be vastly different than in local galaxies. If true, this has a strong impact on the relation between metallicity and UV absorption line properties. In particular, for (optically thick) IS absorption lines, this correlation is dominated by velocity dispersion, which is broadening the lines. However, the velocity dispersion is not only set by the stellar mass of a galaxy (and therefore metallicity) but also by its star formation and phase of evolution. Upcoming facilities like the *JWST* will allow us to test this. In the meantime, local high- $z$  analogs are the best candidates to understand the physics and the relations in very-high-redshift galaxies (see also Faisst et al. 2016).

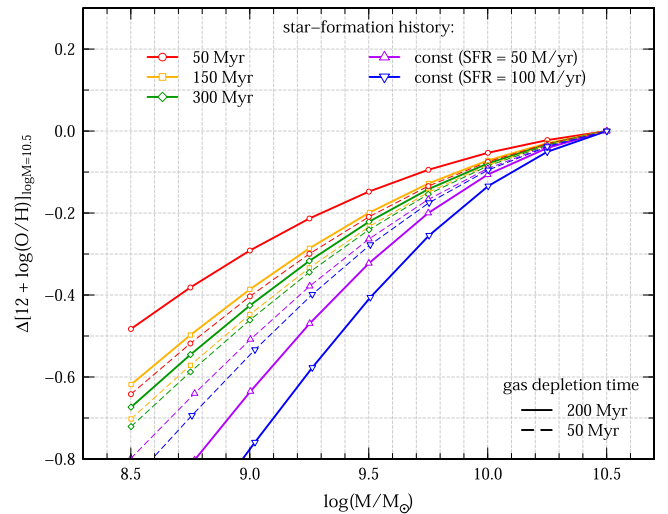


**Figure 11.** Theoretical prediction of the slope of the MZ relation as a function of different SFHs in the “bathtub” formalism. The SFHs are parameterized by  $SFR(t) \propto e^{t/\tau}$  with different  $\tau$  as well as  $SFR(t) = \text{const}$ . We also assume two different gas-depletion times (i.e., inverse of star-formation efficiency) of 50 and 200 Myr (e.g., Scoville et al. 2015b). The MZ relations are normalized to their value at  $\log(M/M_\odot) = 10.5$  in order to remove dependences from other constants (e.g., yield). The slope of the MZ relations significantly change with the assumed SFH. Flatter relations can be achieved by a starburst-like SFH with short  $\tau$ .

Keeping these caveats in mind, there might also be interesting physical reasons responsible for the weakening of the MZ relation. Several studies indicate that high- $z$  galaxies behave differently and live in different environments than the average galaxy at low  $z$ . They are characterized by a clumpy mode of star formation (Förster Schreiber et al. 2011), caused by strong gas inflows in the dense and gas-rich high- $z$  universe. They show shorter gas depletion times (e.g., Scoville et al. 2015b; Silverman et al. 2015) and a mass build-up on shorter timescales indicated by their high specific SFRs (Stark et al. 2013; Speagle et al. 2014; Faisst et al. 2016). All these different properties of high- $z$  galaxies and their surroundings have an impact on the observed MZ relation. In the following, we use a “bathtub model” approach (e.g., Lilly et al. 2013) to investigate this in more detail.

In brief, we assume a similar set of differential equations as set up in Feldmann (2015). We assume a mass-dependent mass loading factor as described in their Equation (24), which is motivated by hydrodynamical simulations of galactic winds (Hopkins et al. 2012). For the gas depletion time  $t_{\text{depl}}$ , we assume 200 and 50 Myr independent of redshift (e.g., Scoville et al. 2015b). We let the galaxies evolve according to two different sets of SFHs in the  $\sim 1$  billion years to redshift  $z = 5$ . We assume three exponential increasing SFHs with  $\tau = 50, 150,$  and  $300$  Myr, as well as a constant SFH with  $SFR_0 = 50 M_\odot \text{ yr}^{-1}$  and  $SFR_0 = 100 M_\odot \text{ yr}^{-1}$ . Figure 11 shows how the slope of the MZ relation derived from our simple bathtub model is affected by the different SFHs and gas-depletion times. From our simple model, we expect that the slope becomes shallower for starburst-like SFHs (i.e., exponentially increasing with a short  $\tau$ ) as well as for short gas-depletion times as long as  $\tau > t_{\text{depl}}$ . We note that the uncertainty in our data does not allow us to constrain the model’s parameters. Rather, the model should give an idea of what could happen at high  $z$  and what we expect in terms of the evolution of the MZ relation to high redshifts.

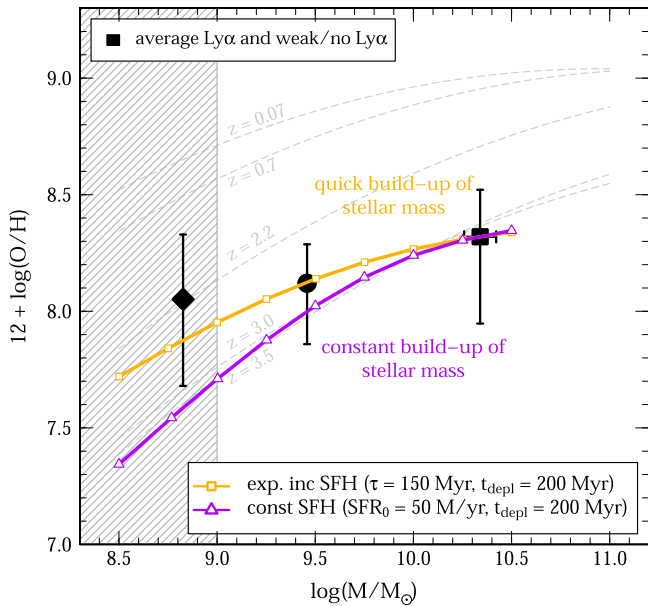


**Figure 12.** Average MZ relation for our  $z \sim 5$  galaxies along with two models with exponential increasing ( $\tau = 150$  Myr,  $t_{\text{depl}} = 200$  Myr) and constant ( $\text{SFR} = 50 M_{\odot} \text{ yr}^{-1}$ ) SFHs, normalized to  $\log(M/M_{\odot}) \sim 10.4$  (see Figure 11). Our derived MZ relation at  $z \sim 5$ , if real, requires star formation on short timescales, while at lower redshifts (e.g.,  $z \sim 3\text{--}3.5$ ) a shallower SFH is favored. This hints at a rapid growth of massive galaxies in the early epochs of our universe.

Keeping this in mind, Figure 12 shows a subset of models normalized to  $\log(M/M_{\odot}) = 10.5$  along with our estimates at  $z = 5$  and data at lower redshifts. We pick a constant SFH with  $\text{SFR}_0 = 50 \text{ Myr}$  and  $t_{\text{depl}} = 200$  Myr as well as an exponentially increasing SFH with  $\tau = 150$  Myr and  $t_{\text{depl}} = 200$  Myr, matching well the data at  $z = 5$  and  $z = 3.5$ , respectively. A shallower MZ relation is therefore in agreement with the mass build-up in high- $z$  galaxies on short timescales, as expected from their high specific SFRs.

A mass build-up on a short timescale might also prevent the galaxy population as a whole from having a clear relation between stellar mass and dust obscuration along the line of sight within the galaxy. It indicates that the processes that form the galaxies at high  $z$  are more stochastic than at low  $z$ . In the same stellar mass range (i.e., without dependence on mass), the dust and metallicity properties of these galaxies vary substantially. We indeed see indications of this in our sample consisting of galaxies with strong Ly $\alpha$  emission as well as galaxies showing weak or no Ly $\alpha$  emission. Since Ly $\alpha$  is resonantly scattered off neutral gas (that is correlated with dust), weak Ly $\alpha$  emission is indicative of a higher dust column density and therefore a higher metal content of these galaxies. This is in agreement with our findings: weak-Ly $\alpha$ -emitting galaxies tend to have marginally stronger UV absorption (Figure 5), that is, a higher metallicity that is similar to  $z \sim 2$  galaxies (Figure 9) compared to strong-Ly $\alpha$ -emitting galaxies. Furthermore, their less-prominent P-Cygni profile is indicative of an older stellar population; hence they could be more evolved than strong-Ly $\alpha$ -emitting galaxies. Since they do have the same mass distribution and redshift as galaxies with strong Ly $\alpha$  emission, they might have experienced a more gradual formation over a longer timescale, closer to the SFHs of galaxies at  $z = 2\text{--}3$ . We would expect longer  $e$ -folding times

for their mass build-up instead of a quick ramping up, and therefore our bathtub model would predict a more significant MZ relation. There are hints of a more significant MZ relation for weak-Ly $\alpha$ -emitting galaxies in our data, but its large uncertainties prevent us from strictly proving this prediction.

Summarizing, we do expect a weakening of the MZ relation at  $z = 5$  if galaxies are formed on fast, exponential timescales with  $e$ -folding times of 100–200 Myr. The weaker MZ relation indicated by our data is supported by the lack of a significant correlation between stellar mass and dust attenuation. Furthermore, the  $z = 5$  galaxy population is diverse, including a range of metallicities, including lower than  $z \sim 3\text{--}3.5$  and as high as  $z = 2$  galaxies. The big diversity might be indicative of a process of galaxy formation at  $z = 5$  being more stochastic and diverse. This could weaken the clear relations seen at lower redshifts.

## 7. SUMMARY AND CONCLUSIONS

Emission features employed to measure metallicity in  $z \lesssim 3$  galaxies are redshifted out of the wavelength range of current ground-based detectors. It is therefore not possible to probe the metal content of  $z > 3$  galaxies using these lines until the advent of *JWST*. Instead, we have to rely on alternative methods. In this paper, we use the correlation between metallicity and the EW of rest-frame UV absorption features to infer the metal properties of a large sample of galaxies at  $z \sim 5$ .

We compile a sample of  $\sim 50$  local galaxies and calibrate the relation between metallicity and the most prominent absorption features seen in high- $z$  galaxies (Si IV, C IV, Si III, C II). For the first time, we verify this relation to hold up to  $z \sim 3$  by using a sample of  $\sim 30$  galaxies at  $z = 2\text{--}3$  with metallicity measurements from strong optical emission lines. We then apply (correcting for various biases) this method to a spectroscopic sample of 224 galaxies at  $z \sim 5$ , which is constructed to be as diverse as possible in terms of physical properties of the galaxies. Most importantly, this sample allows us to investigate directly the properties of galaxies with strong Ly $\alpha$  emission as well as those with no or weak Ly $\alpha$  emission.

The findings of this paper are the following:

1. The average population of  $z \sim 5$  galaxies shows gas-phase metallicities very similar to  $z \sim 3\text{--}3.5$  galaxies at a fixed stellar mass, but a factor of about two lower metal content compared to  $z \sim 2$ .
2. We find hints of a positive trend between metallicity and UV continuum slope, and the negative trend between metallicity and SFR agrees. If true, this would very well fit what is expected from low redshifts and could indicate that the dependence of dust and metallicity holds up to  $z \sim 5$ , as well as a scenario where star formation is held up by a strong inflow of pristine (metal-poor) gas.
3. We do not see a significant correlation between dust attenuation and stellar mass (as seen at lower redshifts). Also, we do not find a significant relation between stellar mass and metallicity at  $z \sim 5$  within the uncertainties of our measurements for Ly $\alpha$ -emitting galaxies.
4. We find a large diversity in our galaxy sample at  $z \sim 5$ . Galaxies with weak or no Ly $\alpha$  emission ( $\sim 25\%$  at  $\log(M/M_{\odot}) > 10.0$ ) show a slightly higher metal content compared to strong-Ly $\alpha$ -emitting galaxies. This is most

significant for high masses. This can be interpreted as them being more evolved than systems with strong Ly $\alpha$  emission, which is supported by the less-prominent P-Cygni profiles in their stacked spectra.

Taking our results at face value, there are multiple reasons for the lack of an apparent MZ relation at  $z \sim 5$ . Most of these can be reduced to uncertainties in the measurements of the various parameters (in particular metallicity and stellar mass). However, if real, it allows us to constrain the build-up of stellar mass in galaxies at these early epochs. Using a “bathtub model” approach, we find that a shallow MZ relation can be caused by a fast build-up of stellar mass on the order of only a couple 100 Myr. The fast formation of these galaxies might cause a more stochastic distribution of the properties and therefore weaken the possible relations that are seen at lower redshifts. This is supported by the observation of our set of galaxies devoid of Ly $\alpha$  emission that show a factor of two increased average metal content at the same stellar masses than the rest of our sample at  $z \sim 5$ .

For firm conclusions, the reliability of these measurements has to be improved, and systematic effects have to be minimized. This can be done by (1) using stellar population models with a better treatment of the ISM effects to investigate in more depth the age and metallicity and (2) targeting specifically low-metallicity galaxies at lower redshifts to increase the leverage of the EW versus metallicity relation at the low-metallicity end. The galaxy sample presented in this work spans a wide range of physical parameters and stems from a spectroscopic survey that is as complete as possible. This sample is therefore ideal to follow up by *JWST*, which will be able to measure metallicities for these galaxies and verify our results.

We would like to acknowledge the support of the Keck Observatory staff who made these observations possible as well as Micaela Bagley, Janice Lee, and David Sobral for valuable discussions. We also would like to thank the referee for valuable comments that have improved this paper. A.F. acknowledges support from the Swiss National Science Foundation. The authors wish to recognize and acknowledge the very significant cultural role and reverence that the summit of Mauna Kea has always had within the indigenous Hawaiian community. We are most fortunate to have the opportunity to conduct observations from this mountain.

## APPENDIX VELOCITY OFFSETS DUE TO OUTFLOWS AND WINDS IN $z \sim 5$ GALAXIES

Winds and outflows are common in local starburst and star-forming galaxies at high redshifts and are related to their metal content. Direct evidence for strong outflows and winds in our sample at  $z \sim 5$  is the strong P-Cygni profiles seen in the C IV and Si IV absorption lines (see Figure 5). Different velocity offsets of the galaxies can cause biases and uncertainties in the measurements of the spectral properties on stacked spectra. For example, this can lead to a broadening of absorption features or their complete removal in the stacked spectra. In this section, we provide estimates of velocity offsets due to outflows and winds in our  $z \sim 5$  galaxies that we use to quantify the uncertainties in the EW measurements. Moreover, these

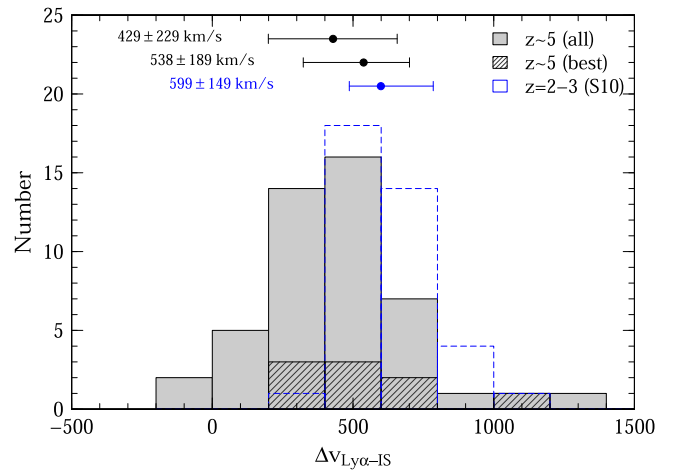


**Figure 13.** Distribution of velocity offset between Ly $\alpha$  and IS absorption features for galaxies for which both can be measured (all galaxies: light gray; most secure: dark gray). The data from Steidel et al. (2010) at  $z = 2-3$  is shown in dashed blue.

measurements are useful for further studies of this galaxy sample in the future.

### A.1. Velocity Offsets between IS Lines and Ly $\alpha$

Figure 13 shows the velocity offset of the IS absorption lines with respect to Ly $\alpha$  ( $\Delta v_{\text{Ly}\alpha-\text{IS}}$ ) for individual galaxies for which both Ly $\alpha$  and IS absorption is observed. We find a mean velocity offset of  $\Delta v_{\text{Ly}\alpha-\text{IS}} \sim 538 \pm 189 \text{ km s}^{-1}$  for the most secure IS absorption redshifts and  $\Delta v_{\text{Ly}\alpha-\text{IS}} \sim 429 \pm 229 \text{ km s}^{-1}$  if including all galaxies with measured IS absorption. This is broadly consistent with the measurements of  $\sim 50$  galaxies at  $z \sim 2-3$  (Steidel et al. 2010) shown by the blue dashed histogram. The  $\Delta v_{\text{Ly}\alpha-\text{IS}}$  measurements on the composite spectrum for single absorption features are given in Table 3 and range between  $-1000$  and  $-380 \text{ km s}^{-1}$ . The uncertainties of these measurements are conservatively estimated as  $\pm 100 \text{ km s}^{-1}$ , which is twice a resolution element ( $100 \text{ km s}^{-1}$  or  $0.5 \text{ \AA}$ ). The median over all absorption lines ( $\sim 570 \text{ km s}^{-1}$ ) is consistent with the values for individual galaxies shown in Figure 13.

### A.2. Systemic Velocity Offsets of Ly $\alpha$ and IS Lines

Finding the absolute velocity components of Ly $\alpha$  and the absorption lines ( $\Delta v_{\text{sys}}$ ) with respect to systemic  $1300 \text{ \AA}$  consisting of Si III, C III, and O I is clearly detected in the composite spectrum. Unfortunately, these lines are blended, and therefore an exact systemic redshift cannot be assigned. In addition, because of the different velocity offsets of the individual galaxies, the stacking in the Ly $\alpha$  rest frame changes the measured systemic redshift from the true.

Since our galaxies on average show  $\Delta v_{\text{Ly}\alpha-\text{IS}}$  values similar to the Steidel et al. (2010) sample at  $z = 2-3$  (Figure 13), we use their galaxies (which have systemic redshift from H $\alpha$  measurements) to investigate the systematic biases when measuring  $\Delta v_{\text{sys}}$  from the composite spectrum. These simulations are detailed in the next section, and we summarize the main points in the following. First, from Steidel et al. (2010) we know that the point of largest absorption of the Si III/C III/O I complex is a good tracer of the systemic redshift. We then use the systemic redshifts obtained for eight of our galaxies

from the measurement of the C II fine-structure line at  $157.7 \mu\text{m}$  using the *Atacama Large Millimeter/Sub-millimeter Array* (ALMA) to verify our approach (Capak et al. 2015). An extensive Monte Carlo simulation using the Steidel et al. (2010) sample as input finally shows that there is a bias toward bluer velocity offsets for Ly $\alpha$  and IS absorption of  $40 \text{ km s}^{-1}$  and  $90 \text{ km s}^{-1}$ , respectively. This is mainly due to the stacking of galaxies with different  $\Delta v_{\text{Ly}\alpha\text{-IS}}$  in the Ly $\alpha$  rest frame, as mentioned above.

The uncorrected and corrected (in brackets) velocity offsets and the uncertainties from the Monte Carlo run are listed in Table 3 for the different spectral lines. Note that the velocity offset of the He II emission is consistent with the systemic velocity measured by the blended O I line; this is an independent verification of the calibration of the systemic rest frame. We find bias-corrected velocities for IS absorption features of  $-200 \pm 90 \text{ km s}^{-1}$  and for Ly $\alpha$  of  $340 \pm 170 \text{ km s}^{-1}$  measured on the composite spectrum. Both the Ly $\alpha$  and IS absorption velocity offsets are in agreement with studies at  $z = 2\text{--}3$  ( $\sim -160 \text{ km s}^{-1}$  and  $\sim 450 \text{ km s}^{-1}$ , respectively; Steidel et al. 2010), suggesting similar wind properties of these galaxies.

### A.3. Biases in the Measurement of Velocity Offsets on a Composite Spectrum

The systemic redshift of individual spectra cannot be measured because of their low S/N. On the other hand, several photospheric lines are detected in the composite spectrum (the Si III/C III/O I line complex). These are, however, blended and might be offset from the true because of the stacking of galaxies with different velocity properties.

We investigate these effects by using a sample of 38  $z = 2\text{--}3$  galaxies observed by Steidel et al. (2010). These galaxies have UV spectra similar to ours (in particular similar  $\Delta v_{\text{Ly}\alpha\text{-IS}}$ ) and in addition are observed in H $\alpha$ , from which systemic redshift can be measured. First, the analysis by Steidel et al. shows that the O I absorption line is a very good tracer of the systemic redshift measured by H $\alpha$  if the deepest absorption of the Si III/C III/O I line complex is assigned to O I. This observation can in addition be tested by a set of eight galaxies at  $z \sim 5$  with Ly $\alpha$  emission, which are observed with ALMA and have a derived systemic redshift from the [C II] fine-structure line at  $157.7 \mu\text{m}$  (Capak et al. 2015). We stack these eight galaxies in the Ly $\alpha$  rest frame and measure a velocity offset between Ly $\alpha$  and O I of  $160 \pm 120 \text{ km s}^{-1}$ . This is in excellent agreement with the true Ly $\alpha$  velocity offset with respect to systemic redshift (measured by the [C II] at  $157.7 \mu\text{m}$ ), which we measure to be  $-170 \pm 70 \text{ km s}^{-1}$ . The velocity offset between Ly $\alpha$  and IS lines is  $490 \pm 200 \text{ km s}^{-1}$ , consistent with the median of the distribution shown in Figure 13.

The biases and uncertainties of the velocity measurements using the blended O I line on the composite spectrum are investigated by a Monte Carlo simulation. We create 38 model galaxies with two different fiducial absorption lines (O I for the photospheric/systemic line and the redder line of the Si IV doublet as the IS absorption line) as well as Ly $\alpha$  based on the velocity offsets shown in Figure 2 of Steidel et al. (2010). The lines are parameterized by a Gaussian with different FWHM and rest-frame EW values. For Ly $\alpha$  we choose basis values EW =  $10 \text{ \AA}$  and FWHM =  $2 \text{ \AA}$ , and for the IS and photospheric lines we choose basis values EW = (4, 2)  $\text{ \AA}$  and FWHM = (6, 8)  $\text{ \AA}$ , respectively. Furthermore, we add random

noise to each of the model spectra such that the S/N is between 2 and 10, as for our real galaxies.

We then create 200 composite spectra from the 38 model galaxies, each time changing their EW and FWHM by 20% as well as their noise level (between S/N of 2 and 10). On these we measure the velocity offsets of our fiducial Ly $\alpha$  and IS absorption line assuming the fiducial O I line is tracing the systemic redshift. This simulation shows that we are able to recover the input velocity offsets reasonably well within  $100 \text{ km s}^{-1}$  from the true. However, we find a systematic bias for both  $\Delta v_{\text{Ly}\alpha}$  and  $\Delta v_{\text{IS}}$  toward the blue by  $40 \text{ km s}^{-1}$  and  $90 \text{ km s}^{-1}$ , respectively. Also, the uncertainties on the measurements from the Monte Carlo sampling are on the order of  $\pm 180 \text{ km s}^{-1}$  and  $\pm 230 \text{ km s}^{-1}$ , respectively. The corrected velocity values are given in Table 3 and are used to estimate the effect of velocity offsets on the measurement of EWs.

## REFERENCES

- Allen, M. G., Dopita, M. A., & Tsvetanov, Z. I. 1998, *ApJ*, 493, 571  
 Ando, M., Otho, K., Iwata, I., et al. 2007, *PASJ*, 59, 717  
 Andrews, B. H., & Martini, P. 2013, *ApJ*, 765, 140  
 Arnouts, S., Cristiani, S., Moscardini, L., et al. 1999, *MNRAS*, 310, 540  
 Arnouts, S., Le Floch, E., Chevillard, J., et al. 2013, *A&A*, 558, A67  
 Atek, H., Siana, B., Scarlata, C., et al. 2011, *ApJ*, 743, 121  
 Belli, S., Jones, T., Ellis, R. S., & Richard, J. 2013, *ApJ*, 772, 141  
 Bothwell, M. S., Maiolino, R., Kennicutt, R., et al. 2013, *MNRAS*, 433, 1425  
 Bouché, N., Dekel, A., Genzel, R., et al. 2010, *ApJ*, 718, 1001  
 Brandt, J. C., Heap, S. R., Beaver, E. A., et al. 1994, *PASP*, 106, 890  
 Bruzual, G., & Charlot, S. 2003, *MNRAS*, 344, 1000  
 Calzetti, D., Armus, L., Bohlin, R. C., et al. 2000, *ApJ*, 533, 682  
 Capak, P., Aussel, H., Ajiki, M., et al. 2007, *ApJS*, 172, 99  
 Capak, P. L., Carilli, C., Jones, G., et al. 2015, *Natur*, 522, 455  
 Castor, J. I., Abbott, D. C., & Klein, R. I. 1975, *ApJ*, 195, 157  
 Chabrier, S. 2003, *Archives de Pédiatrie*, 10, 168  
 Cowie, L. L., Songaila, A., Hu, E. M., & Cohen, J. G. 1996, *AJ*, 112, 839  
 Davé, R., Finlator, K., & Oppenheimer, B. D. 2012, *MNRAS*, 421, 98  
 de Barros, S., Schaerer, D., & Stark, D. P. 2014, *A&A*, 563, A81  
 De Lucia, G., Kauffmann, G., & White, S. D. M. 2004, *MNRAS*, 349, 1101  
 Edmunds, M. G. 1990, *MNRAS*, 246, 678  
 Edmunds, M. G., & Pagel, B. E. J. 1984, *MNRAS*, 211, 507  
 Eldridge, J. J., & Stanway, E. R. 2009, *MNRAS*, 400, 1019  
 Eldridge, J. J., & Stanway, E. R. 2012, *MNRAS*, 419, 479  
 Ellison, S. L., Patton, D. R., Simard, L., & McConnachie, A. W. 2008, *ApJL*, 672, L107  
 Erb, D. K., Shapley, A. E., Pettini, M., et al. 2006, *ApJ*, 644, 813  
 Faber, S. M., Phillips, A. C., Kibrick, R. I., et al. 2003, *Proc. SPIE*, 4841, 1657  
 Faisst, A. L., Capak, P., Hsieh, B. C., et al. 2016, *ApJ*, 821, 122  
 Feldmann, R. 2015, *MNRAS*, 449, 3274  
 Ferland, G. J., Korista, K. T., Verner, D. A., et al. 1998, *PASP*, 110, 761  
 Finkelstein, S. L., Papovich, C., Salmon, B., et al. 2012, *ApJ*, 756, 164  
 Finlator, K., & Davé, R. 2008, *MNRAS*, 385, 2181  
 Fitzpatrick, E. 1989, in *IAU Symp. 135, Interstellar Dust*, ed. L. J. Allamandola, & A. G. G. M. Tielens (Cambridge: Cambridge Univ. Press), 37  
 Förster Schreiber, N. M., Shapley, A. E., Erb, D. K., et al. 2011, *ApJ*, 731, 65  
 Franceschini, A., Rodighiero, G., Cassata, P., et al. 2006, *A&A*, 453, 397  
 Gallazzi, A., Bell, E. F., Zibetti, S., Brinchmann, J., & Kelson, D. D. 2014, *ApJ*, 788, 72  
 Gam, T., & Best, P. N. 2010, *MNRAS*, 409, 421  
 Garnett, D. R. 2002, *ApJ*, 581, 1019  
 Gavazzi, G., & Scodreggio, M. 1996, *A&A*, 312, L29  
 González, V., Bouwens, R., Illingworth, G., et al. 2014, *ApJ*, 781, 34  
 Harms, R. J., Beaver, E., Burbidge, E. M., et al. 1979, *Proc. SPIE*, 183, 74  
 Harwit, M., & Brisbin, D. 2015, *ApJ*, 800, 91  
 Heckman, T. M., González-Delgado, R., Leitherer, C., et al. 1997, *ApJ*, 482, 114  
 Heckman, T. M., Robert, C., Leitherer, C., Garnett, D. R., & van der Rydt, F. 1998, *ApJ*, 503, 646  
 Heinis, S., Buat, V., Béthermin, M., et al. 2014, *MNRAS*, 437, 1268  
 Henry, A., Scarlata, C., Domínguez, A., et al. 2013, *ApJL*, 776, L27  
 Hopkins, P. F., Quataert, E., & Murray, N. 2012, *MNRAS*, 421, 3522

- Hsieh, B.-C., Wang, W.-H., Hsieh, C.-C., et al. 2012, *ApJS*, 203, 23
- Hsu, L.-T., Salvato, M., Nandra, K., et al. 2014, *ApJ*, 796, 60
- Ilbert, O., Arnouts, S., McCracken, H. J., et al. 2006, *A&A*, 457, 841
- Ilbert, O., McCracken, H. J., Le Fèvre, O., et al. 2013, *A&A*, 556, A55
- Ilbert, O., Salvato, M., Le Floch, E., et al. 2010, *ApJ*, 709, 644
- James, B. L., Pettini, M., Christensen, L., et al. 2014, *MNRAS*, 440, 1794
- Jones, T., Stark, D. P., & Ellis, R. S. 2012, *ApJ*, 751, 51
- Kennicutt, R. C., Jr. 1998, *ARA&A*, 36, 189
- Kewley, L. J., & Dopita, M. A. 2002, *ApJS*, 142, 35
- Kewley, L. J., & Ellison, S. L. 2008, *ApJ*, 681, 1183
- Kinney, A. L., Bohlin, R. C., Calzetti, D., Panagia, N., & Wyse, R. F. G. 1993, *ApJS*, 86, 5
- Köppen, J., Weidner, C., & Kroupa, P. 2007, *MNRAS*, 375, 673
- Kornei, K. A., Shapley, A. E., Martin, C. L., et al. 2012, *ApJ*, 758, 135
- Laigle, C., McCracken, H. J., Ilbert, O., Hsieh, P., & Capak, P. 2016, *ApJ*, in press (arXiv:1604.02350)
- Lara-López, M. A., Bongiovanni, A., Cepa, J., et al. 2010, *A&A*, 519, A31
- Larson, R. B. 1974, *MNRAS*, 169, 229
- Leitherer, C., Tremonti, C. A., Heckman, T. M., & Calzetti, D. 2011, *AJ*, 141, 37
- Lequeux, J., Peimbert, M., Rayo, J. F., Serrano, A., & Torres-Peimbert, S. 1979, *A&A*, 80, 155
- Lilly, S. J., Carollo, C. M., Pipino, A., Renzini, A., & Peng, Y. 2013, *ApJ*, 772, 119
- Lilly, S. J., Le Fèvre, O., Renzini, A., et al. 2007, *ApJS*, 172, 70
- Maeder, A., & Conti, P. S. 1994, *ARA&A*, 32, 227
- Maier, C., Lilly, S. J., Carollo, C. M., Stockton, A., & Brodwin, M. 2005, *ApJ*, 634, 849
- Maier, C., Lilly, S. J., Ziegler, B. L., et al. 2014, *ApJ*, 792, 3
- Maier, C., Ziegler, B. L., Lilly, S. J., et al. 2015, *A&A*, 577, A14
- Maiolino, R., Nagao, T., Grazian, A., et al. 2008, *A&A*, 488, 463
- Mallery, R. P., Mobasher, B., Capak, P., et al. 2012, *ApJ*, 760, 128
- Mannucci, F., Cresci, G., Maiolino, R., et al. 2009, *MNRAS*, 398, 1915
- Mannucci, F., Cresci, G., Maiolino, R., Marconi, A., & Gnerucci, A. 2010, *MNRAS*, 408, 2115
- Maraston, C., Nieves Colmenárez, L., Bender, R., & Thomas, D. 2009, *A&A*, 493, 425
- Martin, C. L., Shapley, A. E., Coil, A. L., et al. 2012, *ApJ*, 760, 127
- Masters, D., & Capak, P. 2011, *PASP*, 123, 638
- Masters, D., McCarthy, P., Siana, B., et al. 2014, *ApJ*, 785, 153
- McCracken, H. J., Milvang-Jensen, B., Dunlop, J., et al. 2012, *A&A*, 544, A156
- McLean, I. S., Steidel, C. C., Epps, H. W., et al. 2012, *Proc. SPIE*, 8446, 0
- Mehlert, D., Noll, S., Appenzeller, I., et al. 2002, *A&A*, 393, 809
- Nagao, T., Maiolino, R., & Marconi, A. 2006, *A&A*, 459, 85
- Oke, J. B., & Gunn, J. E. 1983, *ApJ*, 266, 713
- Onodera, M., Carollo, C. M., Lilly, S., et al. 2016, *ApJ*, in press (arXiv:1602.02779)
- Oteo, I. 2014, *A&A*, 572, L4
- Pagel, B. E. J., Edmunds, M. G., Blackwell, D. E., Chun, M. S., & Smith, G. 1979, *MNRAS*, 189, 95
- Pérez-González, P. G., Rieke, G. H., Villar, V., et al. 2008, *ApJ*, 675, 234
- Pettini, M., & Lipman, K. 1995, *A&A*, 297, L63
- Pettini, M., Rix, S. A., Steidel, C. C., et al. 2002, *ApJ*, 569, 742
- Pettini, M., Steidel, C. C., Adelberger, K. L., Dickinson, M., & Giavalisco, M. 2000, *ApJ*, 528, 96
- Pipino, A., Lilly, S. J., & Carollo, C. M. 2014, *MNRAS*, 441, 1444
- Rix, S. A., Pettini, M., Leitherer, C., et al. 2004, *ApJ*, 615, 98
- Roseboom, I. G., Bunker, A., Sumiyoshi, M., et al. 2012, *MNRAS*, 426, 1782
- Sahu, M. S., & Blades, J. C. 1997, *ApJL*, 484, L125
- Salim, S., Lee, J. C., Davé, R., & Dickinson, M. 2015, *ApJ*, 808, 25
- Salpeter, E. E. 1955, *ApJ*, 121, 161
- Sanders, R. L., Shapley, A. E., Kriek, M., et al. 2015a, *ApJ*, 816, 23
- Sanders, R. L., Shapley, A. E., Kriek, M., et al. 2015b, *ApJ*, 799, 138
- Santini, P., Ferguson, H. C., Fontana, A., et al. 2015, *ApJ*, 801, 97
- Santini, P., Maiolino, R., Magnelli, B., et al. 2014, *A&A*, 562, A30
- Savage, B. D., & Mathis, J. S. 1979, *ARA&A*, 17, 73
- Savaglio, S., Glazebrook, K., Abraham, R. G., et al. 2004, *ApJ*, 602, 51
- Savaglio, S., Glazebrook, K., Le Borgne, D., et al. 2005, *ApJ*, 635, 260
- Schaerer, D., & de Barros, S. 2009, *A&A*, 502, 423
- Scoville, N., Aussel, H., Brusa, M., et al. 2007, *ApJS*, 172, 1
- Scoville, N., Faisst, A., Capak, P., et al. 2015a, *ApJ*, 800, 108
- Scoville, N., Sheth, K., Aussel, H., et al. 2015b, arXiv:1505.02159
- Shapley, A. E., Reddy, N. A., Kriek, M., et al. 2015, *ApJ*, 801, 88
- Silverman, J. D., Daddi, E., Rodighiero, G., et al. 2015, *ApJL*, 812, L23
- Sobral, D., Best, P. N., Matsuda, Y., et al. 2012, *MNRAS*, 420, 1926
- Sommariva, V., Mannucci, F., Cresci, G., et al. 2012, *A&A*, 539, A136
- Speagle, J. S., Steinhardt, C. L., Capak, P. L., & Silverman, J. D. 2014, *ApJS*, 214, 15
- Stark, D. P., Schenker, M. A., Ellis, R., et al. 2013, *ApJ*, 763, 129
- Steidel, C. C., Erb, D. K., Shapley, A. E., et al. 2010, *ApJ*, 717, 289
- Steidel, C. C., Rudie, G. C., Strom, A. L., et al. 2014, *ApJ*, 795, 165
- Steinhardt, C. L., Speagle, J. S., Capak, P., et al. 2014, *ApJL*, 791, L25
- Storchi-Bergmann, T., Calzetti, D., & Kinney, A. L. 1994, *ApJ*, 429, 572
- Tremonti, C. A., Heckman, T. M., Kauffmann, G., et al. 2004, *ApJ*, 613, 898
- Walborn, N. R., MacKenty, J. W., Saha, A., White, R. L., & Parker, J. W. 1995, *ApJL*, 439, L47
- Wilkins, S. M., Coulton, W., Caruana, J., et al. 2013, *MNRAS*, 435, 2885
- Wuyts, E., Kurk, J., Förster Schreiber, N. M., et al. 2014, *ApJL*, 789, L40